

MASSIVELY-PARALLEL DIRECT NUMERICAL SIMULATION OF
GAS TURBINE ENDWALL FILM-COOLING CONJUGATE HEAT TRANSFER

A Thesis

by

CHARLES MICHAEL MEADOR

Submitted to the Office of Graduate Studies of
Texas A&M University
in partial fulfillment of the requirements for the degree of

MASTER OF SCIENCE

December 2010

Major Subject: Mechanical Engineering

MASSIVELY-PARALLEL DIRECT NUMERICAL SIMULATION OF
GAS TURBINE ENDWALL FILM-COOLING CONJUGATE HEAT TRANSFER

A Thesis

by

CHARLES MICHAEL MEADOR

Submitted to the Office of Graduate Studies of
Texas A&M University
in partial fulfillment of the requirements for the degree of

MASTER OF SCIENCE

Approved by:

Chair of Committee,	Andrew Duggleby
Committee Members,	J.C. Han
	Theofanis Strouboulis
Head of Department,	Dennis O'Neal

December 2010

Major Subject: Mechanical Engineering

ABSTRACT

Massively-Parallel Direct Numerical Simulation of
Gas Turbine Endwall Film-Cooling Conjugate Heat Transfer. (December 2010)

Charles Meador, B.S., Texas A&M University

Chair of Advisory Committee: Dr. Andrew Duggleby

Improvements to gas turbine efficiency depend closely on cooling technologies, as efficiency increases with turbine inlet temperature. To aid in this process, simulations that consider real engine conditions need to be considered. The first step towards this goal is a benchmark study using direct numerical simulations to consider a single periodic film cooling hole that characterizes the error in adiabatic boundary conditions, a common numerical simplification. Two cases are considered: an adiabatic case and a conjugate case. The adiabatic case is for validation to previous work conducted by Pietrzyk and Peet. The conjugate case considers heat transfer in the solid endwall in addition to the fluid, eliminating any simplified boundary conditions. It also includes an impinging jet and plenum, typical of actual endwall configurations. The numerical solver is NEK5000 and the two cases were run at 504 and 128 processors for the adiabatic and conjugate cases respectively. The approximate combined time is 100,000 CPU hours. In the adiabatic case, the results show good agreement for average velocity profiles but over prediction of the film cooling effectiveness. A convergence study suggests that there may be an area of unresolved flow, and the film cooling momentum flux may be too high. Preliminary conjugate results show agreement with velocity profiles, and significant differences in cooling effectiveness. Both cases will need to be refined near the cooling hole exit, and another convergence study done. The results from this study will be used in a larger case that considers an actual turbine vane and film cooling hole arrangement with real engine conditions.

ACKNOWLEDGMENTS

I would like to acknowledge all the professors and students I was able to work with during my undergraduate career that motivated my interest to continue to learn. I want to thank my research group members for all of their help and support, especially Markus for his continued patience and guidance through my master's career. I thank my advisor, Dr. Andrew Duggleby, for his help and support through out the past few years. Thank you to my parents, friends, and family for their support and to my loving wife, Angie, for always believing in me and continued support.

NOMENCLATURE

Q_{in}	Heat input, by fuel
T_{ad}	Adiabatic wall temperature
T_c	Film cooling exit temperature
T_g	Free stream gas temperature
Tu	Turbulence intensity
U_∞	Free stream velocity
U_m	Mean velocity
V	Velocity
W_{turb}	Work output of the turbine
ΔP	Change in pressure
δ	Boundary layer thickness
δ^*	Displacement thickness
η_{th}	Thermal efficiency, first law efficiency
Re_D	Reynolds number, based on hole diameter $U_\infty D/\nu$
Re_θ	Reynolds number, based on momentum thickness $U_\infty \theta/\nu$
$\overline{u'^2}$	Average fluctuating x velocity squared
$\overline{v'^2}$	Average fluctuating y velocity squared

$\overline{w'^2}$	Average fluctuating w velocity squared
ρ	Density
θ^*	Momentum thickness
ν	Kinematic viscosity
<i>rms</i>	Root mean square
B	Blowing ratio, $\rho_j U_j / \rho_\infty U_\infty$
D	Film cooling hole diameter
DNS	Direct numerical simulation
DR	Density ratio, ρ_j / ρ_∞
DSSN	Downstream Spiral Separation Node
I	Momentum ratio, $\rho_j U_j^2 / \rho_\infty U_\infty^2$
LES	Large eddy simulation
RANS	Reynolds averaged Navier-Stokes
VR	Velocity ratio, U_j / U_∞
CAD	Computer aided drafting
CHT	Conjugate heat transfer
RBM	Recycling boundary condition method

TABLE OF CONTENTS

CHAPTER		Page
I	INTRODUCTION AND LITERATURE REVIEW	1
	A. Gas Turbine Basics	1
	B. Theory of Operation	2
	1. Compressor	3
	2. Combustor	5
	3. Turbine	6
	C. Flow Losses	7
	1. Secondary Flow Losses	8
	D. Cooling Technology	10
	1. Impingement Cooling	11
	2. Rib-Turbulated Cooling	11
	3. Pin Fin Cooling	12
	4. Film-Cooling	12
	E. Computation Methods	13
	F. Literature Review	15
II	PROBLEM DESCRIPTION	19
	A. Objective Statement	19
	B. Geometry	19
	1. Domain Parameters	20
	2. Boundary Conditions	22
	3. Turbulence Generation	22
	C. Mesh Generation Technique	26
	1. Mesh Computational Basics	26
	2. Complex Geometry Limitations	28
	3. Gambit NEU	29
	4. Matlab Code	31
	a. readingNEU	31
	b. orderElemPts	32
	c. orderMidPts	33
	d. getConnectivity	33
	e. getBC	33
	f. getCurvedSides	34

CHAPTER	Page
g. periodic	34
h. recycle	35
D. Calibration Validation	35
III RESULTS	39
A. Convergence Study	39
B. Average Velocity Profiles	41
C. Film Cooling Effectiveness	44
D. Future Considerations	49
1. Current Study	49
2. Larger Study	50
IV CONCLUDING REMARKS	52
REFERENCES	54
VITA	57

LIST OF TABLES

TABLE		Page
I	Free stream boundary layer characteristics 2D upstream of film cooling hole leading edge from experiments.	22
II	Coolant to free stream ratio parameters	23

LIST OF FIGURES

FIGURE		Page
1	Example aircraft gas turbine engine	3
2	Compressor stage stator and rotor	4
3	Combustion chamber diagram	6
4	Turbine blade passage example	7
5	Secondary flow dynamics in turbine passage	9
6	Internal cooling technology in a turbine blade	10
7	Jet impingement diagram for array configuration	11
8	Rib-Turbulated flow separation and schematic	12
9	Comparison of computational methods	14
10	History of turbine blade design compared to inlet temperatures	16
11	Computational domain adiabatic and conjugate cases	20
12	Geometric parameters pertinent to the domain	21
13	Eddy inlet condition for free stream	24
14	Intensity control and check flow diagram	25
15	Comparison of global and local mesh descriptions	27
16	Example of global, local, and connectivity matrices	28
17	Preferred NEK format for local element ordering and mesh data	32
18	REA file boundary conditions and connectivity	34
19	REA file curved side data example	35

FIGURE	Page
20	Illustration of periodic boundary condition routine 36
21	Experimental setup for conjugate impinging jet 37
22	Convergence plot for adiabatic case 40
23	Downstream spiral separation node vortex 41
24	Adiabatic film cooling hole exit velocity profiles 42
25	Jetting phenomena in film cooling hole 43
26	DSSN vortex visible in conjugate case 44
27	Adiabatic film cooling hole free stream velocity profiles 45
28	Development of span wise velocity profiles 46
29	Average adiabatic temperature distribution at the wall 47
30	Adiabatic temperature distribution at centerplane 47
31	Temperature distribution in the endwall conjugate case 48
32	Film cooling effectiveness comparisons 48
33	Near wall mesh around film cooling hole 49
34	Future simulation domain 51

CHAPTER I

INTRODUCTION AND LITERATURE REVIEW

A. Gas Turbine Basics

Gas turbine engines are the technical name for what is commonly referred to as a jet engine. Air is the working fluid in the engine, and a combustor burns fuel to provide energy for thrust. Jet propulsion is not the only use of gas turbines however. Power production facilities or large manufacturing sites may use gas turbines for power production. Using a gas turbine for power production has the advantage of size compared to a typical steam power plant in that it does not take up as much space. Gas turbines are also becoming popular among automobile researchers, however typical driving conditions experienced in everyday life require a quick response from the engine. This is still an issue with gas turbines that automobile researchers are addressing.

Regardless of the application, the engineer's primary role in the design of gas turbine engines is to maximize the efficiency, while minimizing the cost. This requires a delicate balance between performance, reliability, and safety. Design processes require trade-offs to satisfy each of these areas, and any improvement in one area will decrease the time and cost in another. For engineers, this means performance and efficiency.

Efficiency can have many meanings depending on the application. For gas turbines, or any thermodynamic heat engine, the cycle efficiency is defined as what you

The journal model is *IEEE Journal of Oceanic Engineering*.

put into the system (cost) versus what you get out of the system (want):

$$\eta_{th} = \frac{want}{cost} = \frac{W_{turb}}{Q_{in}}. \quad (1.1)$$

The cost is the energy content of the fuel that is injected into the engine. The ‘want’ is the power produced by the turbine which can be used depending on the application. For aircraft propulsion the desired output is thrust, and the efficiency is defined differently. Typical thermal efficiencies for gas turbines range from 30-40% with regeneration techniques pushing efficiencies close to 60%. Regeneration means that exhaust air from the turbine is used to preheat air entering the combustor resulting in less fuel input.

Similar to the cycle efficiency, each gas turbine component also has an efficiency. For a turbine this is defined as the actual power produced versus the maximum possible. Considering only the aircraft industry, an increase in turbine efficiency of just 1% spread across all airlines and their fleets equates to billions of dollars in savings. This would have tremendous impact in both aerospace and industrial applications. To do this it is necessary to explore and characterize the various thermo-fluid dynamics that occur in all aspects of gas turbine design.

The following section describes the main components in gas turbine engines, and how they operate. With this knowledge, primary and secondary flow losses that effect the turbine efficiency can be addressed.

B. Theory of Operation

Figure 1 shows a diagram of the new Rolls Royce Trent 1000 turbo fan engine which will be used on Boeing’s new 787 Dreamliner aircraft, courtesy of Rolls-Royce.com [1]. It will be used to help explain the various components.

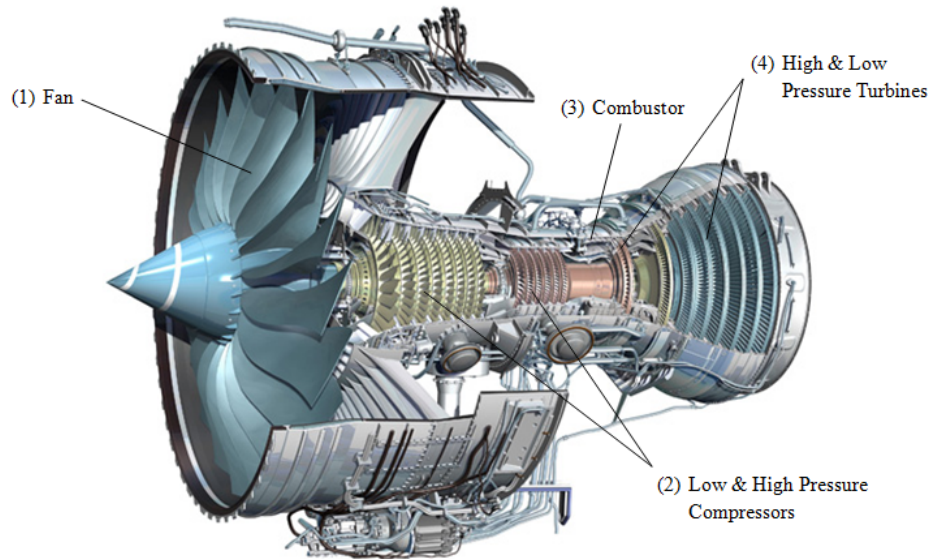


Fig. 1. Example aircraft gas turbine engine. The Rolls Royce Trent 1000 Turbofan Engine, used with written permission from Rolls-Royce.com [1]. The major components are labeled.

1. Compressor

The compressor is the first major component in any gas turbine engine and is labeled (2) in Figure 1. The objective for a compressor is to increase the air pressure before entering the combustion chamber. Compressing air is an unnatural process, meaning it requires work input to occur. An analogy given by Rolls-Royce is trying to sweep water uphill [1]. The required power is taken from the turbine as it extracts energy from the flowing exhaust gases. In typical commercial aircraft engines the first thing one sees is actually the fan, not the compressor. The fan produces large amounts of air flow around the engine which is combined with the turbine exhaust gas to thrust the aircraft forward. This is known as by-pass. By-pass air also reduces exhaust noise and improves the overall thrust efficiency.

The flow resulting from the compressor blade design is responsible for the increase

in pressure. The basic physical concept used by compressors can be understood by Bernoulli's equation:

$$\frac{\Delta P}{\rho} + \frac{V^2}{2} = \text{constant}, \quad (1.2)$$

which relates the pressure and velocity, and ρ is the fluid density. This implies that a decrease in velocity results in an increase in pressure. To decrease the velocity, the area that the fluid flows through must increase; similar to a diffuser. A diffuser is the opposite of a nozzle in which the fluid is accelerated by decreasing the area. Figure 2 shows an example blade design for one stage. A stage refers to a stator vane and a rotor blade. The stator is a stationary blade that sets the inflow for the rotor blades, increases the pressure and keeps the air from following the rotation along the axis. The rotor blades rotate from the power transmitted by the turbine. Although the air pressure increases as it passes through the blade channel, the air will not move by itself. The turbine rotates the compressor, causing the blades to impart a force on the air to move it. The area increase through compressor blades is very subtle due

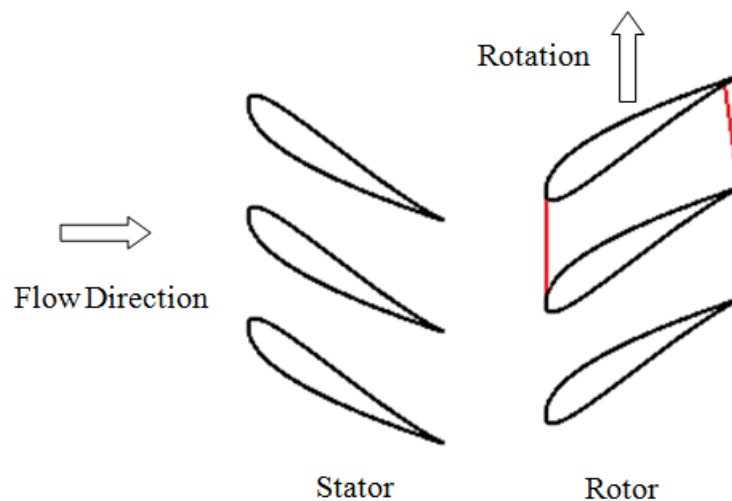


Fig. 2. Compressor stage stator and rotor. The flow flow area at the rotor tail is larger than at the rotor leading edge, denoted by the two red lines.

to the small deflections. This is to reduce the effects of flow losses in which the air flow reverses direction on the blade surface and detaches. This is more likely to occur when decelerating a flow and is undesirable because it diminishes the compressor and overall engine efficiency. Also, because the deflections need to be small, this requires many compressor stages to obtain the desired compression ratio.

2. Combustor

The combustor is where the fuel is injected into the air stream as it leaves the compressor. This is labeled as (3) in Figure 1. A larger image of a combustor appears in Figure 3. The combustor takes in high pressure air from the compressor, mixes fuel with the air, then ignites the mixture to produce very high temperature and high pressure gas for the turbine. The airspray nozzle consists of multiple vane swirlers that “twist” the air as it enters the combustion chamber. This helps mix the air fuel mixture. The igniter is located just downstream of the spray nozzle. The greater the combustor can raise the temperature of the gas from the environment, the more power the turbine can produce as a result. However, this is limited by the thermal and mechanical properties of the materials for the combustor and turbine blades. The gas temperature of the combustion products for modern combustion chambers average 1600°C and may peak above 2000°C , while materials used for the combustors and turbines melt around 1200°C [1]. Therefore it is necessary to cool the combustor walls as well as the gas temperature leaving the combustor.

To cool the hot gas stream to a temperature suitable for the turbine inlet, “cooler” air that bypasses the combustor from the compressor is introduced into the combustion chamber through dilution holes. Cooling techniques for the materials will be discussed in the Cooling Technology section that follows. The “cooler” air is a relative term because the air from the compressor is itself around 700°C [1]. The dilution air

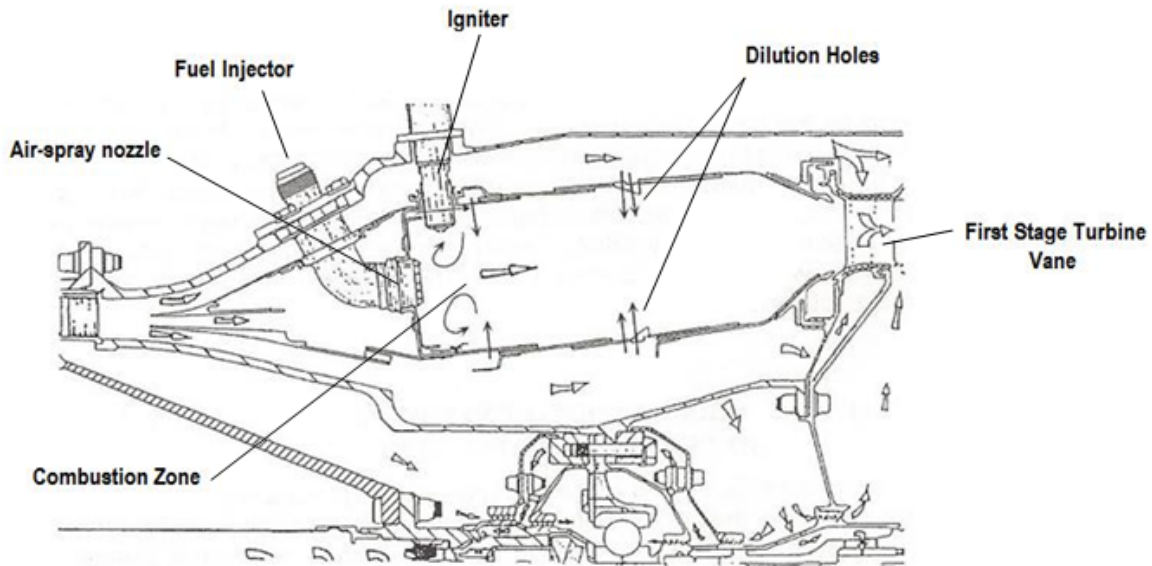


Fig. 3. Combustion chamber diagram. The major components are labeled, modified from Ames et al. [2].

cools the gas temperature to an acceptable and uniform temperature for the turbine. It also helps to reduce carbon dioxide and nitric oxide emissions to the environment by diluting the concentrations.

3. Turbine

The turbine is the component responsible for extracting energy from the combustion gases, and is labeled (4) in Figure 1. It does this through a series of stages consisting of stator and rotor blades similar to the compressor. However, the turbine blades objective is the opposite of the compressor; it wants to accelerate and expand the flow rather than decelerate and compress it. Like the compressor, this is accomplished by the dynamics of the flow resulting from the turbine blade geometry. A typical turbine blade arrangement appears in Figure 4. As the flow moves through the turbine passage, the cross section gets smaller. As discussed earlier this results in

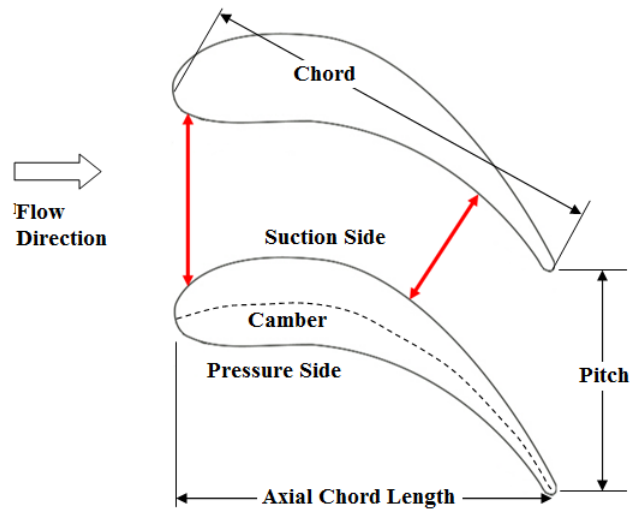


Fig. 4. Turbine blade passage example. It is apparent that the area decreases through the passage.

a loss of pressure, and an increase in velocity. Each stage therefore extracts energy from the flowing fluid by expanding it, and lowering the pressure. The energy that is extracted occurs in the form of mechanical rotation because the blades deflect the flow angle. This principle is known as the conservation of angular momentum. A familiar example is to stick your hand out a car window when it is moving. As the air expands through each stage it progressively loses energy as it cools. Because of this, each turbine stage will progressively have larger deflection angles which is limited because of flow separation.

The following section discusses flow losses that are typical in the turbine stages.

C. Flow Losses

Unlike the cycle efficiency, the efficiency of the turbine is defined as the actual power produced compared to the isentropic power. This power is compared to the fuel input to give the cycle efficiency. The isentropic power assumes that no energy is lost by

heat and irreversibilities, such as friction, are eliminated. In reality, all devices will have some irreversibility. Flow losses that occur during each stage result in pressure losses that can not be converted to useful energy. These losses can be categorized into five main losses: Profile losses, trailing edge thickness loss, secondary losses, trailing edge mixing, and exit losses [3].

Profile losses are affected by geometric factors such as chord-spacing ratios, thickness-chord ratios, and surface roughness effects. Trailing edge thickness loss involves the wake region behind each blade that results from the blade thickness. Trailing edge mixing refers to the ejection of cooling air within the turbine blade through the trailing edge. This helps reduce the thickness loss by providing mass flow into the wake region, but mixing cooler air with the hot gas dissipates energy in the main flow. Exit losses are associated with kinetic energy loss when the flow angle at the exit is different than 90° . Secondary flow losses are specific to this study and will be explained in further detail in the following section.

1. Secondary Flow Losses

Secondary flow losses describe the loss in total pressure resulting in changes in flow dynamics near the turbine hub and the casing compared to the core flow. Near the casing, along the top of the blade, fluid particles on the pressure side jump to the suction side creating the trailing tip vortex. This induces a drag force which must be overcome by additional convective forces that result in pressure loss [3]. Near the hub the fluid flow is dependent on the boundary layer that forms along the turbine endwall. As the boundary layer approaches the leading edge of the turbine vane it stagnates and causes an increase in pressure that is locally higher at the stagnation point than near the wall. This is seen in figure 5.

As a result, gas in the free stream wants to move towards the lower pressure

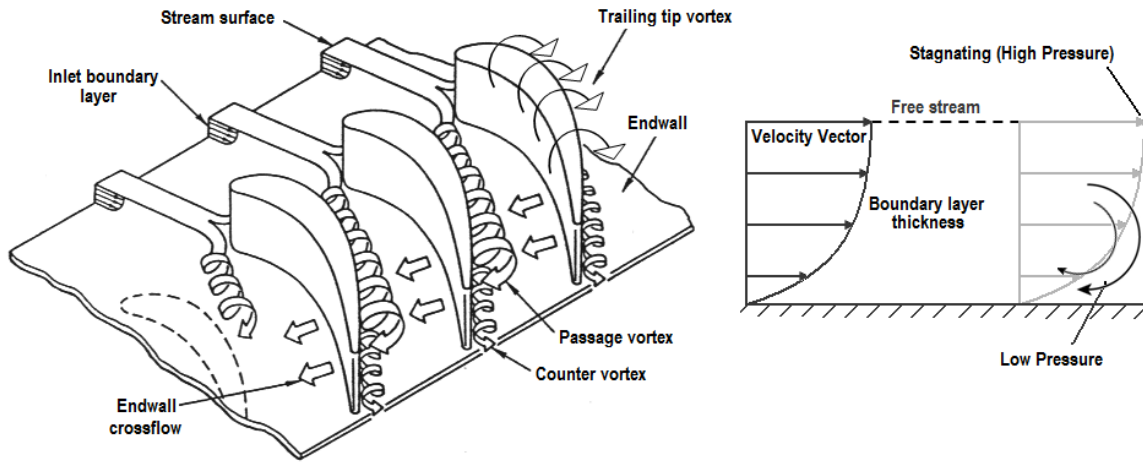


Fig. 5. Secondary flow dynamics in turbine passage. (Left) The trailing tip vortex and horseshoe vortex secondary losses are shown, modified from [4]. (Right) The formation of the horseshoe vortex caused by the stagnating boundary layer. Higher velocity in the free stream coming to rest causes the pressure to be higher than near the wall, inducing the vortex motion shown.

region near the wall. This causes the boundary layer vorticity to reorganize into a coherent structure [5] called the horseshoe vortex which wraps around the pressure and suction side. This vortex is responsible for pressure losses due to the additional convective forces needed to overcome the structure. The hot free stream gas that is driven to the wall surface is also responsible for high thermal stresses due to the high intensity and unsteady nature of the vortex. This reduces the lifetime of the turbine blades and in some circumstances may cause pitting at the leading edge where the material melts.

Therefore, the vortex structure not only decreases the efficiency, but has the potential to cause a catastrophic failure. This is completely undesirable and many techniques have been employed to reduce the impact of the horseshoe vortex [6]. Because the secondary flows influence the efficiency and heat transfer, it is necessary

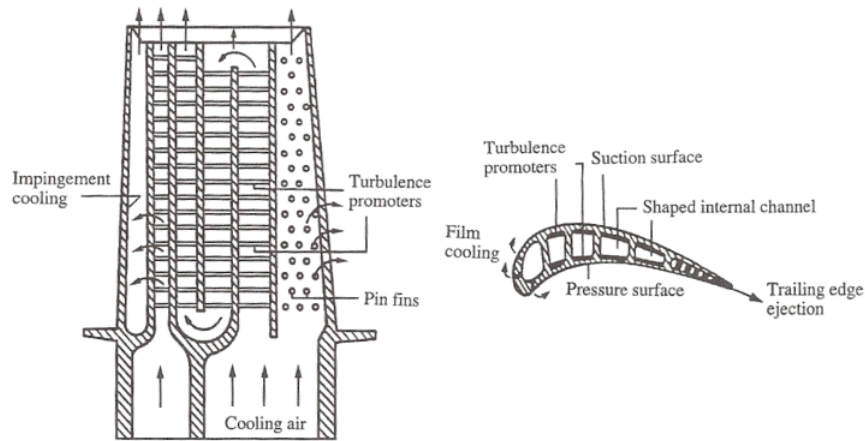


Fig. 6. Internal cooling technology in a turbine blade. Image used from Han [7]. Impingement and film cooling are also used on the endwall.

to discuss cooling techniques that are used in gas turbine engines. These cooling techniques must compete against the secondary flows to protect the turbine surfaces, and their configurations are dependent on these flows. The following sections give an overview of the main cooling techniques.

D. Cooling Technology

The combustion exit temperature is often above the melting point of the materials used in the turbine stages. The following sections explain the main cooling techniques used in the turbine endwall and blades. Figure 6 shows an example of the internal cooling arrangement for a high pressure turbine vane. It is important to note that these cooling techniques are also used on the endwall, as well as the combustor. Film cooling and impingement cooling are used on the endwall and are the primary focus of this study.

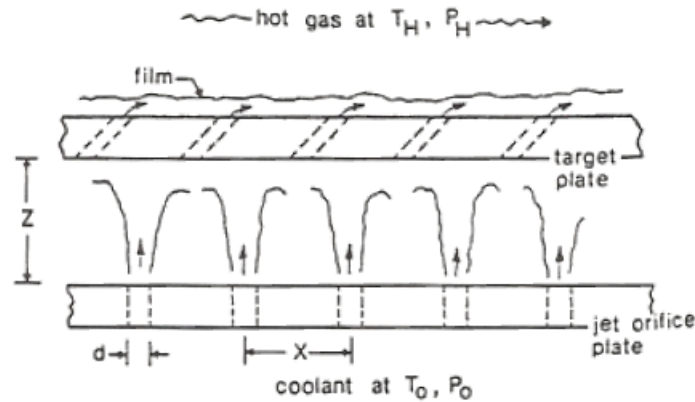


Fig. 7. Jet impingement diagram for array configuration. Image used from Hollworth [9]. Impingement provides high heat transfer coefficients but weakens the structure [8].

1. Impingement Cooling

Impingement cooling provides some of the highest heat transfer coefficients due to the high turbulent structures that develop after the impinging process. However, fabricating the impingement holes weakens the structure and is only used in areas of very high thermal loads [8]. In the turbine blade, this is the leading edge as indicated in Figure 6. For endwall cooling, the jet impinges on the wall underside into a plenum before it is used for film cooling on the external surfaces. Figure 7 shows an array configuration for endwall film cooling and jet impingement.

2. Rib-Turbulated Cooling

Rib turbulated cooling is indicated by the turbulence promoters in Figure 6. These ribs line the internal channels inside the turbine blades. Aside from the increase in surface area in contact with the cooling air, it is thought that the ribs enhance heat transfer by causing the boundary layer to separate and reattach periodically between

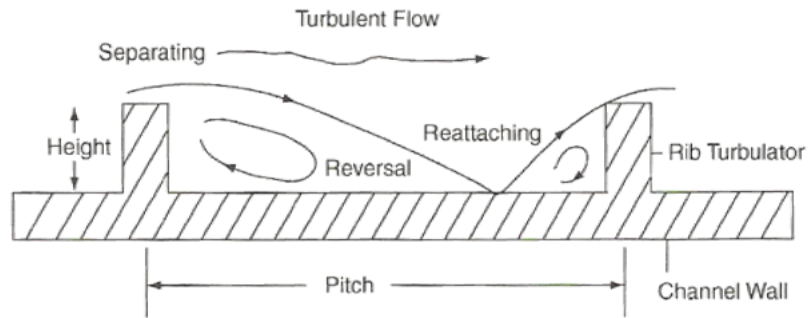


Fig. 8. Rib-Turbulated flow separation and schematic. From Handutta [10].

each rib which enhances the turbulent mixing [8]. This effect can be seen in Figure 8.

3. Pin Fin Cooling

Pin fins are used primarily in the trailing edge region of turbine blades because of difficulty in manufacturing other cooling techniques. Pin fins enhance heat transfer from the blade to the cooling air by increasing the exposed surface area, and promoting turbulence by mixing. Upstream pins shed their wakes into downstream fins and increase the free stream turbulence [8]. Pin fins are not of concern for this study and are included for completeness. Figure 6 shows the pin fins in the trailing edge region.

4. Film-Cooling

Film cooling techniques use an auxiliary fluid at a cooler temperature to coat a surface that is exposed to a high temperature environment. The cooling holes are located at discrete locations along the endwall or turbine blade. Because this study focuses on endwall cooling, the description will address flat surface film cooling. A simple 2D representation of film cooling appears in Figure 7. Film cooling along the endwall must

compete against the horseshoe vortex that forms as a result of secondary flow along the endwall. The configuration of film cooling holes along the surface depends on the dynamics of this vortex and characterizing the secondary flows. Therefore, when simulating film cooling holes it is important to take into account actual operating conditions such as heat conduction through the endwall. This study is the first step and addresses a simple film cooling hole and will be used in future studies that include the horseshoe vortex. The performance for a film cooling hole is often reported in terms of an adiabatic effectiveness. This is a dimensionless temperature that depends on the flow conditions, but the main point is that the solid endwall surface is assumed to be insulated (adiabatic). The adiabatic film cooling effectiveness is defined in equation 1.3:

$$\eta_{ad} = \frac{T_g - T_{ad}}{T_g - T_c}, \quad (1.3)$$

where T_g is the free stream gas temperature, T_c is the average film cooling exit temperature, and T_{ad} is the adiabatic wall temperature. Effectiveness values close to one indicate good film cooling performance, while values near zero indicate poor performance. For a film cooling technique to be considered acceptable it must cool not only in the immediate region of the hole but also downstream. If the endwall is not insulated, the adiabatic wall temperature simply becomes the wall temperature.

E. Computation Methods

The three main techniques used in computational fluid dynamics appear in Figure 9. The plot shows the energy spectra of a turbulent flow field. The abscissa shows the wave number and the ordinate is the energy content at the wave number. Reynolds Averaged Navier-Stokes (RANS) models the entire content of the flow by separating the time dependent velocity fluctuations, and time averaging the Navier-Stokes equa-

tions. This results in additional term called the Reynolds Stress and is unknown. The solution to a RANS model provides average data such as mean velocity, average drag and lift, but requires a model for the fluctuating components.

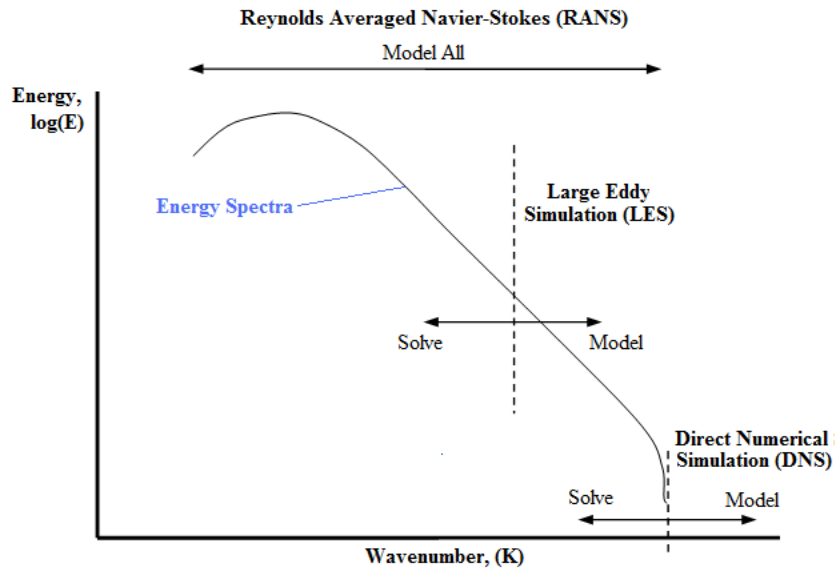


Fig. 9. Comparison of computational methods. Plot gives the energy spectra of a turbulent flow field.

Large Eddy Simulations (LES) are based on Kolmogorov's theory of self similarity. The idea is that the large scales of fluid motion that contain a majority of the energy are dependent on the geometry, but the smaller scales of motion are self-similar, independent of the geometry and therefore can be modelled. A result of an LES formulation is a filtered Navier-Stokes equation in which the small scale motions are filtered out of the solution and instead modelled. This allows a coarser grid which reduces computational costs. The most common LES model is the Smagorinsky sub-grid scale model, but like RANS, also requires model for anisotropy (e.g. near walls) and calibration to experiments. From Figure 9, the LES solves the large scale motions, while modeling small scales.

Direct Numerical Simulations (DNS) solve the Navier-Stokes equations directly without any turbulence model by resolving all the length and time scales of turbulence. The computational costs for a DNS are very high and are limited to certain Reynolds numbers with today's supercomputing capabilities. The following section reviews relevant literature for the present study.

F. Literature Review

The efficiency of a gas turbine engine increases with the combustion exit temperature; however it is often above the melting point of the first stage turbine vanes. Materials for the turbine vanes and endwall are typically cobalt or nickel base super alloys that are coated with ceramic layers, which help mitigate thermal stresses during prolonged operating conditions [11]. Another technique for protecting the endwall is film cooling which uses cooler air from the compressor that is routed through channels to the turbine [8]. This air impinges on the end wall underside into a plenum. From here the air is bled off through cooling holes providing a protective film between the hot gas and metal surface; see Figure 7. By looking at the history of gas turbine blade designs compared to their inlet temperatures in Figure 10, advancements in cooling technology has allowed higher inlet temperatures from the combustor. To continue this trend, further understanding and characterization of turbine film cooling techniques is required that focuses on realistic operating conditions.

Realistic operating conditions for gas turbine engines is a broad statement to describe the actual flow dynamics and heat transfer characteristics that result from the combustion process, such as high free stream turbulence intensity. Turbulent

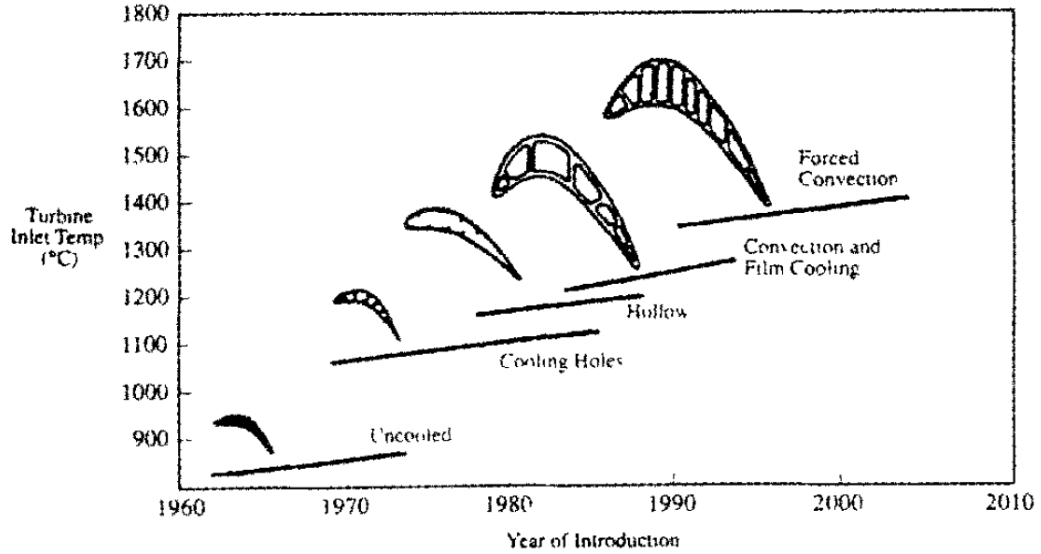


Fig. 10. History of turbine blade design compared to inlet temperatures. From Khan [12]. To continue this trend, research must focus on actual operating conditions.

intensity is defined as:

$$Tu = \frac{\text{rms}}{\text{Mean}} = \frac{\sqrt{1/3(\overline{u'^2} + \overline{v'^2} + \overline{w'^2})}}{U_m}, \quad (1.4)$$

where U_m is the mean velocity, and u'_i are the fluctuating components. High free stream turbulence intensity can be attributed to two aspects in the combustion process: swirlers and dilution holes. The swirlers are guide vanes which “swirl” the compressed air entering the combustion chamber. This helps the air and fuel mix more efficiently and stabilizes the flame. Also, secondary flow dynamics near the endwall degrade the stage efficiency and film cooling performance. Secondary flow will be considered in future studies.

Bogard and Thole [13] suggested that as many as twenty variables affect film cooling effectiveness. As a result, past research has largely focused on a few param-

ters at a time causing geometric and fluid conditions to be simplified. Pietrzyk et al. [14] examined the turbulent characteristics for a jet issued into a cross flow with free stream turbulence less than 0.5%. They present quantitative information of the entire flow field including the upstream and relaxation region downstream of the hole. Actual free stream turbulence levels for first stage turbine vanes range from 5-20% and have been shown to reduce film cooling effectiveness at low blowing ratios [15, 16, 17].

Sinha et al. [18] looked at how the film cooling adiabatic effectiveness varied for different density ratios, and included the use of a plenum. However, no impinging jet was used and the wall was assumed adiabatic. They observed that decreases in the density ratio reduces the film cooling spread and also the averaged effectiveness. Peet et al [19] performed a computational study using a Large Eddy Simulation (LES) to compare turbulent statistics and effectiveness values to [14] and [18] respectively. However, their study did not include the impinging jet or consider conjugate heat transfer to the solid endwall.

Typical thermal boundary conditions for the wall when solving fluid problems is either a constant temperature or constant heat flux. By solving the conjugate solid-fluid problem, the unknown temperature distribution along the interface is determined by solving the solid and fluid equations simultaneously. Dorfman [20] suggests that not using conjugate heat transfer for steady and laminar flow results in only about 4% error. He showed for unsteady flow and as the turbulence increases, the error could be upwards of 30%. Harrison and Bogard [21] attempted to address this as it pertains to film cooling by using an adiabatic case to predict the resulting temperature distributions and heat flux through a conducting metal, and compare it to a conjugate case. The resulting heat flux predictions deviated nearly 300% while non-dimensional temperature distributions on the order of 10%. In gas turbine applications, high turbulence levels and unsteady flow patterns demand considerations of conjugate

heat transfer.

In this present study, a direct numerical simulation is performed on a single, periodic film cooling hole with an impinging jet and plenum using a spectral element solver, NEK5000. The solver has shown sustained performance for over 200,000 processors and, like many spectral solvers, exhibits an exponential convergence rate. The geometry is modeled in Gambit and converted to an acceptable format for the solver. Velocity and turbulence statistics are compared to Pietrzyk [14] and film cooling effectiveness to Sinha [18] by matching the boundary layer parameters observed in the experiments and reported by Peet [19]. The film cooling effectiveness considering conjugate heat transfer, high freestream turbulent intensity, and the effect of the impinging jet will be compared to the results of Pietrzyk, Peet, and Sinha [14, 19, 18].

CHAPTER II

PROBLEM DESCRIPTION

A. Objective Statement

The objective for this study is to characterize the error in current computer models of film cooling which is a cold air barrier between hot gases and material surfaces. Current methods use simplified boundary conditions (adiabatic with no material heat conduction) versus realistic operating conditions seen in gas turbine engines. The results of this study will be used in a complete gas turbine 1st stage vane simulation in a future study that characterizes and reduces flow losses. This industry relevant simulation must include a contoured endwall, conjugate heat transfer, variable density ratios, and high free stream turbulence and large length scales typical of combustor exit profiles. However, the present study must address issues with the simplified boundary conditions before the larger study can be addressed. The following sections introduce the geometric parameters, a technique for the mesh generation, and describe an experimental investigation for validation purposes.

B. Geometry

The following sections describe the geometry used for this study. The domain parameters involve the geometric dimensions and boundary layer parameters. The boundary conditions section specifies values such as the velocity and density ratios, and describes the general boundary conditions including the recycling method. The turbulence generation section highlights the method used to produce turbulent inflow conditions that satisfy conservation of mass and are solutions to the Navier-Stokes equations.

1. Domain Parameters

Two film cooling hole geometries are used for comparison to Peet [19]: an adiabatic case and the conjugate case. The adiabatic case is comparable to [19] in that they report an adiabatic film cooling effectiveness. This essentially means that the end wall is insulated. Also, no impinging jet is used on the adiabatic case. Instead a simple plenum with a mass flux at the inlet is used to control the jet velocity. Figure 11 shows the two cases and the major areas. Each case consists of the same entrance

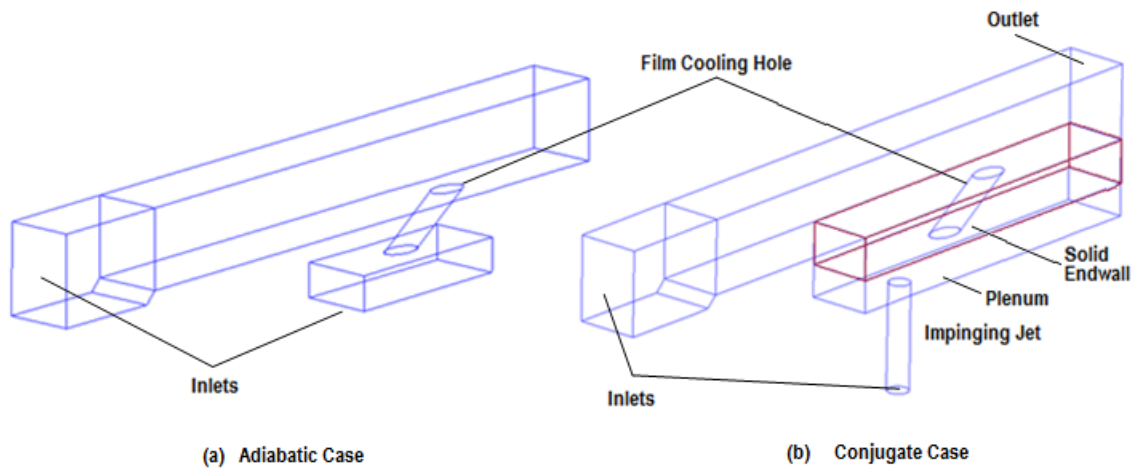


Fig. 11. Computational domain adiabatic and conjugate cases. The major boundary conditions or sections are labeled for clarity.

length, film cooling hole, and a plenum. The adiabatic case does not consider an impinging jet or heat transfer to the solid endwall. The geometries used, and the boundary layer parameters that will be discussed, are taken from [19]. The pertinent geometric parameters appear in Figure 12. The hole length ratio is $L/D = 3.5$, the distance between periodic holes is $P/D = 3.0$, the plenum-jet spacing ratio is $Z/D = 1.5$, film cooling hole angle is 35° , and the velocity ratio (VR) = 0.5. The velocity ratio is defined as the film cooling jet velocity to the free stream velocity. The hole

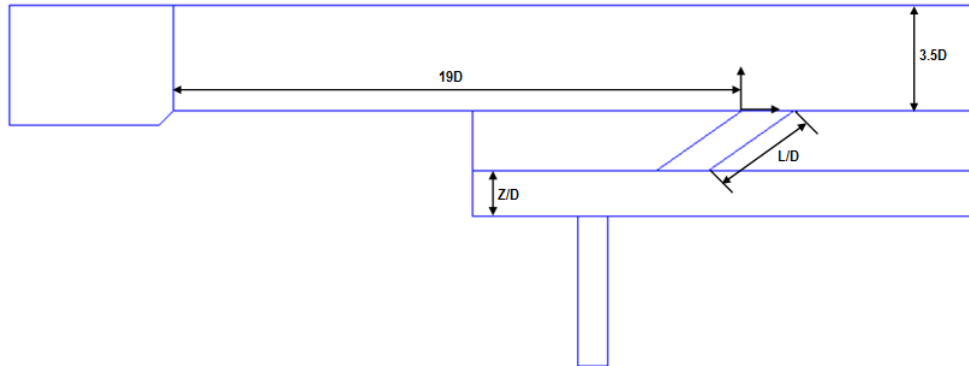


Fig. 12. Geometric parameters pertinent to the domain. These match the description from Pietrzyk et al. [14]

length ratio and angle give an endwall thickness ~ 2.0 . The large entrance length was necessary to match the flat plate boundary layer parameters recorded in the experiments. These appear in Table I. The long entrance length is undesirable as it adds extra computational costs. This will be addressed in the future study: a technique for generating turbulent inflow conditions, with low element count, that may provide correct boundary layer statistics. The boundary layer parameters were measured two diameters upstream of the film cooling hole's leading edge. At this location the dimensionless boundary layer thickness was 0.52 with a Reynolds number, $Re = U_\infty D/\nu$, based on the cooling hole diameter of 16,000. The displacement thickness and momentum thickness were 0.089 and 0.059 respectively, normalized by cooling hole diameter. Boundary layer thickness is defined as the wall normal distance where the velocity is 99% of the average free stream velocity. Displacement thickness can be thought of as a reduction in the effective flow area. It represents the distance the wall would need to be moved to give the same loss in mass flux that the boundary layer gives [22]. Similarly, the momentum thickness represents the equivalent loss in momentum flux if the wall was moved.

Table I. Free stream boundary layer characteristics 2D upstream of film cooling hole leading edge from experiments.

Study	δ/D	δ^*/D	θ/D	Re_θ	Re_D
DNS	0.56	0.0618	0.0382	623	16000
LES [19]	0.47	0.087	0.059	938	16000
Exp. [14].	0.52	0.089	0.059	946	16000

2. Boundary Conditions

The following section describes the boundary conditions and cooling parameters used for the computational study. Two inlets with fixed free stream velocity and temperature are supplied to each computation. The adiabatic case uses a low velocity input to the plenum to give the desired $VR = 0.5$; the fluid in the plenum is essentially stagnant. The conjugate case initializes the impinging jet with Hagen-Poiseuille flow and is recycled to generate a turbulent inflow condition. The recycling method and initial conditions for the inlets are discussed in detail in the Turbulence generation section. Table II gives parameter ratios relevant to the boundary conditions and comparison to the experiments. DR is the density ratio, VR the velocity ratio, B is the blowing ratio, and I is the momentum ratio. Variable density will be considered in a future study.

3. Turbulence Generation

The method for generating turbulent inflow conditions is based on the recycling boundary condition method (RBM). The RBM “copies” the flow conditions at a

Table II. Coolant to free stream ratio parameters. LES from Peet et al. [19], and experiments from Pietrzyk et al [14].

Study	DR	VR	B	I	L/D
DNS	1	0.632	0.632	0.35	3.5
LES [19]	0.95	0.5	0.475	0.2375	3.5
Exp. [14]	1	0.5	0.5	0.25	3.5

downstream location and uses this as the inflow condition. To maintain a divergence free flow, the recycled inlet condition must be scaled such that the volumetric flow rate through the recycling portion is constant. Also a sufficient distance between the inlet plane and recycling plane is needed to prevent the flow from developing any periodic structures. The latter criteria is an issue that needs to be addressed with future studies. The recycling condition alone will not provide turbulent inflow; the flow must be initialized with a velocity field that satisfies the following criteria:

- Solution to Navier-Stokes.
- Satisfies mass conservation (Divergence free).
- Promotes the three characteristics of turbulence: Mixing, Chaos, Vorticity.
- Has large scale spatial fluctuations.

The chaotic nature of the flow field will develop as the solution marches in time. For the free stream inlet, a velocity field is prescribed for the perturbation components that gives a periodic, vortex structure that is a solution to Navier-Stokes, which will be referred to as the Walsh solution [23]. The initial condition propagates with the

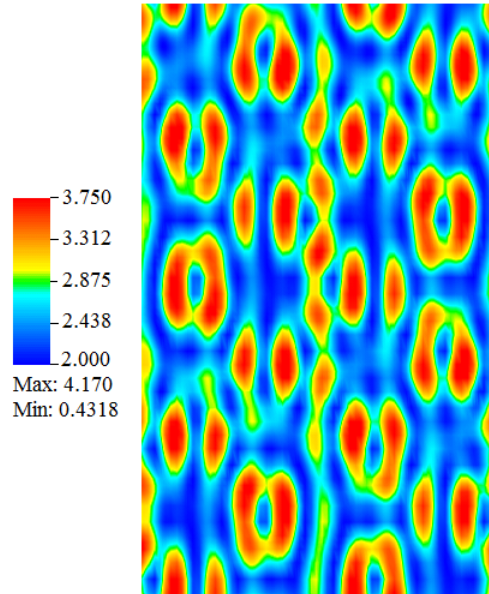


Fig. 13. Eddy inlet condition for free stream. Described by Walsh [23]. The vortex intensity and spacing may be controlled to give desired length scales and turbulence intensity.

free stream velocity which is constant and satisfies the $VR = 0.5$. This eddy solution appears in Figure 13. The larger eddies interact with smaller eddies and give birth to additional vortices as the flow moves in the recycling box. The distance between the recycling and inlet plane allows these structures to develop before being recycled. An issue with this method is that the recycling box is double periodic in y and z . For vorticity production to exist, there must be some shear field present such as a wall. Because the periodic box has no walls viscosity will eventually dampen out any eddies and reduce the turbulence intensity. A solution is to add extra eddies to the inlet plane by introducing a percentage of Walsh solution. However, the percentage of Walsh to add is unknown and may not be constant. To overcome this, an “intensity check” was developed which maintains a desired turbulent intensity level within the

recycling box. The method is based on control theory and uses a proportional-integral-derivative (PID) controller with a single variable. The PID control is a feedback system that checks a desired quantity, and adjusts a parameter until the quantity is met. Figure 14 gives a flow diagram for this process. At each time step the

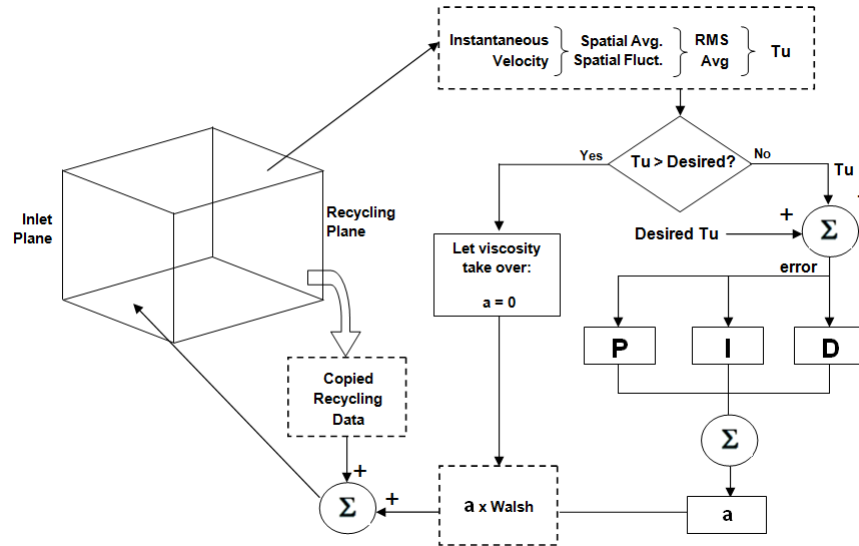


Fig. 14. Intensity control and check flow diagram. The inlet flow is a combination of the recycling plane data and a percentage of eddies from the Walsh solution.

instantaneous velocities are used to find spatial average and fluctuating components in x , y , and z . These are used to find a spatial turbulent intensity value at each time step. If the measured intensity level is larger than the desired, the scaling factor for the added Walsh solution is set to zero and viscosity will dampen eddies until the intensity level drops below the desired. The error between the measured and desired value is used as the input to the controller. The PID constants were determined by trial and error until an acceptable response was observed. Tuning the controller was unnecessary because viscosity is used if the intensity level is too large and not the controller itself. The contributions of the controller are summed and used as the

scaling factor a . The resulting inlet flow is then the sum of the recycling plane data and the Walsh solution scaled by the factor a .

C. Mesh Generation Technique

Creating geometries within NEK5000 (NEK) is difficult for complex geometries, but because the code is open source it is possible to import geometries by some other method if the geometry files can be understood. The geometry file for NEK is called the ‘rea’ file because of the file extension. This file contains mesh coordinate information, curved side data, as well as momentum and thermal boundary conditions. The objective for importing geometries is to understand the rea file parameters, determine acceptable meshing software that can export general data sets, and develop a code capable of converting the general data into an rea file. Before this can be described, issues with creating geometries with NEK itself are discussed to develop the motivation for the alternative code.

1. Mesh Computational Basics

In any computational study, mathematical models are developed that describe the physical processes that govern a type of behaviour. These models are the base for any computational study. The continuous functions, often partial differential equations, that describe the physics are discretized, and converted into algebraic expressions that can be solved with a computer. Often these models are applied to complex geometries which also require discretization called the mesh. Figure 15 shows a simple 2D mesh that will be used to describe how a computational model references the geometry. The description is specific to NEK, but is typical of many solvers. A mesh can be thought of in a global or a local sense. The local node numbering helps determine

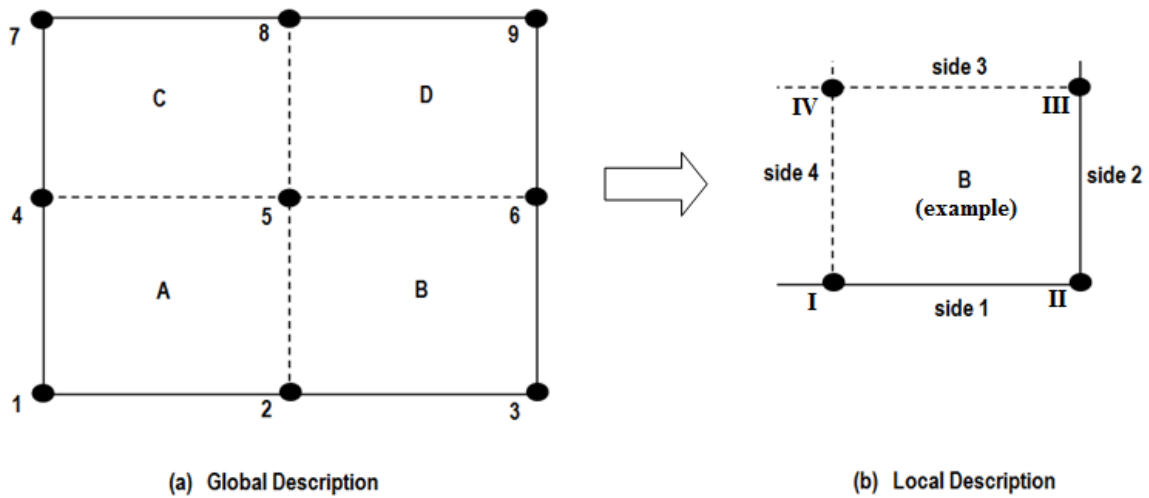


Fig. 15. Comparison of global and local mesh descriptions. (a) Global node numbering for elements A-D and nodes 1-9 (b) Local element node numbering and side definition for a representative element B, with local nodes I-IV.

the connectivity of the mesh (that is which side of element “B” is connected to what other element) and the boundary conditions. The global node numbering links each element to each other. For example local point 1 of element B is global point 2, which is also local point 2 for element A. Side 4 of element B is connected to side 2 of element A. For boundary conditions, sides 1 and 2 of element B are not connected to anything and would need a boundary condition. Figure 16 gives an example of the global points matrix, the local points matrix, and the connectivity matrix. Looking at elements B and D, both share global points 5 and 6 however their local points are different. For element D these points correspond to local points 1 and 2, or side 1. For element B the local points are 3 and 4, or side 3. The connectivity matrix reads “element B Side 3 is connected to element D side 1.”

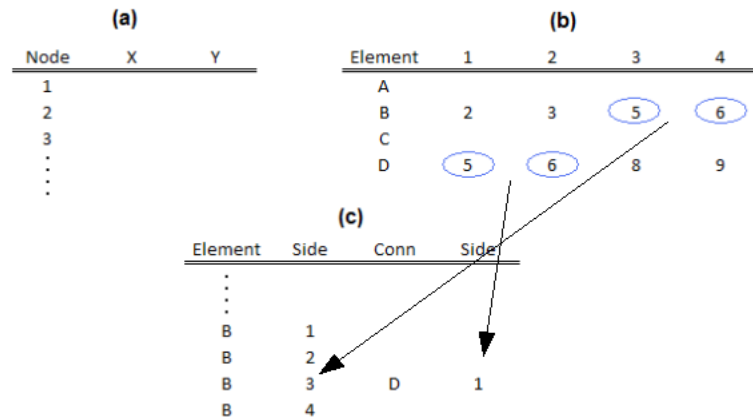


Fig. 16. Example of global, local, and connectivity matrices. (a) Global point matrix (b) Local point matrix links global points to each element (c) Connectivity Matrix

2. Complex Geometry Limitations

PRENEK is the mesh generation code that comes with NEK5000. Aside from POST-NEK, which is for post-processing, it is the only visual interface the user has with NEK. It is used to set up such things as the problem type, fluid properties, and tolerance parameters. It is also used to create the mesh and define boundary conditions. In PRENEK, elements are created individually by clicking the mouse where the corner points should be. There are some routines that can create patterns of elements, refine elements in other areas, and also the option to import an object. An object consists of a text file with the coordinates of a desired shape, such as a turbine blade. The points are imported as an object and the user has the ability to create elements that conform to the shape. However, it still requires clicking the elements one by one. Another drawback is the view orientation is 2D only. For three-dimensional geometries, the mesh has to be created by building layers in a 2D view. For simple geometries, a 2D mesh can be extruded to form a 3D mesh. Applying boundary condi-

tions presents another issue. Boundary conditions can be applied individually to each side of an element, or an entire 2D level can be given the same boundary condition. For 3D geometries, this still requires that each ‘layer’ be addressed separately. It is apparent that for large or complex geometries, these limitations with PRENEK make it very difficult to work with. Because of this, it is necessary to construct a method for importing geometries into NEK that are created with a more user-friendly meshing utility. Several options were explored before deciding on the commercial meshing software Gambit. The following sections detail the use of Gambit, and the general method for converting to an acceptable format for NEK5000.

3. Gambit NEU

The criteria for selecting a meshing utility were the ability to import 3D CAD (Computer Aided Drafting) files, mesh entire volumes at once, apply general boundary conditions to entire surfaces, work with fluid and solid elements for conjugate cases, and a general export format that could be manipulated into a compatible NEK format. Other minor requirements were discovered in the process of understanding NEKs geometry file and will be discussed accordingly. The need to import CAD files arises from the complex geometries seen in gas turbine applications. Many commercial CAD software packages such as Solidworks or PRO Engineer can export CAD files through a Parasolid format. With a proper license, these files can be imported into Gambit. For the current study the geometry was built completely in Gambit because of the relatively simple volumes, however for future studies the geometry will need to be imported by this method.

Meshing an entire volume addresses the issue in PRENEK with creating elements individually for complex shapes. NEK uses hexahedral elements and currently there is no automatic meshing routine for hexahedral. However, if the user splits the geometry

into simple volumes, Gambit can mesh these volumes given certain “mappings” of the volume sides. The volume map ensures that each side has the same number of elements as the opposite side for consistency. This is the major constraint when working with hexahedral elements. Another advantage is Gambit’s ability to create elements with midside-node support. This is important for creating curved sides in NEK. There are different options in NEK for creating curved sides, and the selected option involves this midside node. NEK will fit a parabola through the two edge corner points and the midpoint, creating a curved edge. Each of the elements 12 edges may be curved to form curved surfaces. Because real surfaces are not always parabolas, there will be some error associated with this approximation, however as the mesh is refined this error should diminish to an acceptable value. Boundary conditions can be applied with the zones feature in Gambit. Using a generic description, the user can define the boundary condition type and select the faces corresponding to the boundary condition. This allows the user to apply conditions to entire, generally curvilinear surfaces at once. Gambit will determine which elements and their faces correspond to the boundary condition and output this as a boundary condition section in the data file.

Similarly, the zones feature can be used to distinguish solid and fluid volumes for conjugate heat transfer (CHT) cases in NEK. Creating a CHT case with PRENEK is a complicated task in itself. The user must create the fluid portion separately from the solid portion, and then merge each REA file into one. There is a technical reason for this that deals, however this task will be bypassed with the code described in the following section by defining the solid region in Gambit. Gambit satisfies the requirements needed for converting a general, complex geometry into a NEK format directly. The file that Gambit exports for a generic solver type is called the neutral file (NEU). This file contains global point coordinates, element information linking

the local element points to the global points, and boundary condition information. Element connectivity information is not included. The method for determining the connectivity and a general description of the conversion code is discussed in the following section.

4. Matlab Code

The code used to convert geometries created in Gambit to REA files for use in NEK is written in Matlab. It must read in the neutral file from Gambit and organize the data in a manner that is compatible with NEK. The following briefly describes the overall procedures for creating the REA file for NEK.

The neutral file contains the global points matrix, and a local points matrix. The local points matrix lists the points for each element in terms of the global points. There is no connectivity information so the Matlab code uses these two matrices to determine the connectivity. The connectivity routine consumes 60-80% of the code run time depending on if it is run in parallel. Boundary conditions are manually specified in Gambit, and are included in the neutral file. Each boundary condition is sub divided into its own matrix with a header atop each matrix for the different conditions. The NEU format for the boundary conditions gives the element number, element type, and element face. Element type is an expression to distinguish 2D from 3D, tetrahedral from hexahedral among others and is not used in this case. The actual procedure for converting the NEU file to an rea file is too detailed for to describe here. Instead, each routine is summarized in terms of its function as it relates to the code.

a. readingNEU

All the pertinent data required for the rea that is located in the NEU is read into matlab by this routine. It determines how many elements, grid points, boundary

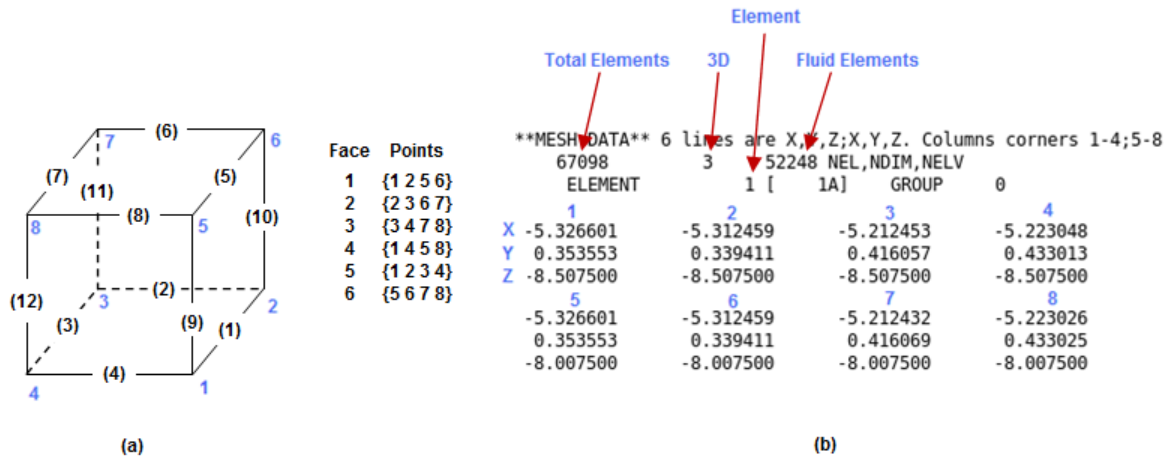


Fig. 17. Preferred NEK format for local element ordering and mesh data. (a) Preferred NEK format for corner points, midpoints, and faces (b) Example of the mesh data portion in an rea file

condition sets, and fluid zones are necessary. It also restructures the global and local point matrices. The local point matrix in the NEU file contains midpoint information as well. The midpoints are removed and stored as a separate matrix, leaving only the corner points. This is also where the user inputs the boundary conditions used by NEK in place of the generic conditions specified in Gambit.

b. orderElemPts

Order Element Points restructures the local point matrix that was read by the previous routine. It reorganizes the corner points into the preferred NEK format shown in Figure 17. The local point matrix is used to write the “mesh data” in the rea file, using the global coordinates in the local point positions.

c. `orderMidPts`

This routine restructures the midpoint matrix into the preferred NEK format. In Figure 17, the numbered edges correspond to the midpoint numbers. Midpoints are used to generate curved sides in NEK.

d. `getConnectivity`

The connectivity routine examines only the local point matrix from the `orderElemPts` routine. This matrix contains only corner points, and is ordered in NEK format. Using the method depicted in Figure 16, this routine constructs the connectivity matrix (c) by searching through the local point matrix (b) to determine which points are also used in other elements. The corresponding points are then matched to a face. Each element and side is considered individually because Gambit does not guarantee that elements will always be oriented in a uniform and consistent manner. This is the reason the connectivity routine takes 60-80% of the code run time.

e. `getBC`

The boundary condition routine takes in matrices from ‘readingNEU’ that describe the boundary conditions. They include the element, face, and type. In NEK, boundary conditions are combined into the connectivity matrix. This routine searches the connectivity routine for the corresponding element and face, then places the boundary type at this location. Figure 18 gives an example of the boundary condition and connectivity information in the `rea` file. The letter ‘E’ stands for element and specifies that the particular face is connected to another element face, which is shown in columns 3 and 4. Note that for boundary conditions there is no connectivity.

```

Connected
**** BOUNDARY CONDITIONS ****
**** FLUID BOUNDARY CONDITIONS ****
E 1 600.00 3.00000 0.00000 0.00000 0.00000
E 1 7.00 4.00000 0.00000 0.00000 0.00000
E 1 2.00 1.00000 0.00000 0.00000 0.00000
Wall W 1 0.00 0.00000 0.00000 0.00000 0.00000
Inlet v 1 0.00 0.00000 0.00000 0.00000 0.00000
E 1 31.00 5.00000 0.00000 0.00000 0.00000
      element      face

```

Fig. 18. REA file boundary conditions and connectivity. Momentum boundary conditions and element connectivity for element 1.

f. getCurvedSides

The curved sides routine uses the ordered midpoint matrix to determine the element edges that are actually curved. Every element is given midpoint data from Gambit, however not every edge is curved. The method for distinguishing the curved from straight edges is based on fitting a circle through the three points that make up each edge: two corner points and the midpoint. The user specifies a radius limit in the inputs section. If the radius of the fitted circle exceeds this limit, the routine ignores the edge. Otherwise the midpoint coordinates, element, and edge number are written to a matrix that will create the curved side portion of the rea, which appears in Figure 19.

g. periodic

The periodic routine is an optional routine if periodic boundary conditions are specified. During the readingNEU routine, the user is prompted to specify the NEK boundary conditions. If periodic is entered, the user must also specify the periodic direction and a tolerance. The periodic routine considers only the elements with a periodic boundary condition. Figure 20 helps illustrate the method. The periodic di-

```

# of curved sides
**** CURVED SIDE DATA ****
9996 Curved sides follow IEDGE,IEL,CURVE(I),I=1,5, C CURVE
4 1 -5.277429 0.396677 -8.507500 0.000000 0.000000 m
8 1 -5.277419 0.396684 -8.007500 0.000000 0.000000 m
4 2 -5.164390 0.461940 -8.507500 0.000000 0.000000 m
8 2 -5.164397 0.461937 -8.007500 0.000000 0.000000 m
4 3 -5.038311 0.495722 -8.507500 0.000000 0.000000 m
8 3 -5.038332 0.495720 -8.007500 0.000000 0.000000 m
side element X Y Z
midpoint routine

```

Fig. 19. REA file curved side data example. The X,Y,Z gives the coordinates of each midpoint on the given element and side.

rection tells the routine to ignore these coordinate points since they will be the same for periodic faces. The four corner points are used to find the centroid of a face. The remaining elements and faces in the periodic list are searched to determine which centroid matches within the user specified tolerance. When it is found, both elements are removed from the list. A drawback is the tolerance must be smaller than any periodic element dimension.

h. recycle

The recycle routine is used for recycling boundary condition set up. The routine creates a special connectivity matrix that links the inlet plane to a specified recycle plane downstream. This matrix is read during runtime to alter the connectivity in NEK.

D. Calibration Validation

High-data density experimental results is needed to validate the conjugate heat transfer simulations. Since most reported experimental data in literature is only at a few discrete points, the data density is not adequate for a full calibration and so an

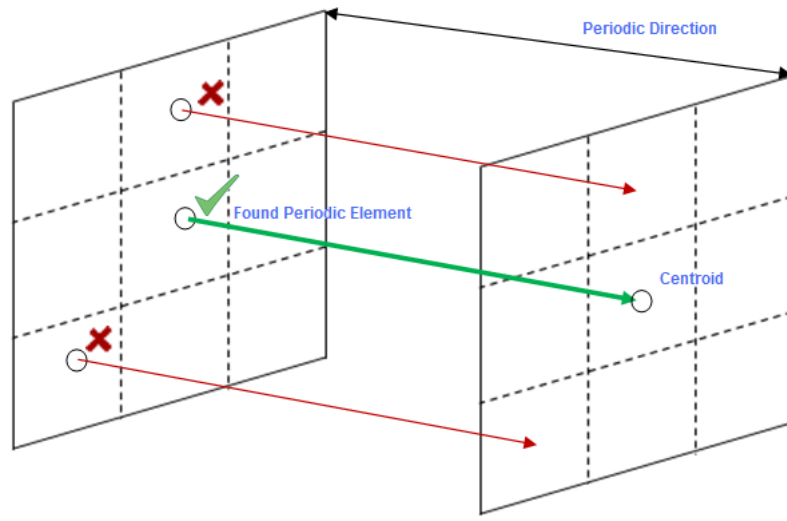


Fig. 20. Illustration of periodic boundary condition routine.

experiment was designed in-house to provide validation.

An air jet impinging on a thick aluminium plate was selected as the test case. The Nusselt number distribution along the impinging surface was the parameter for comparison. To estimate the Nusselt number required knowledge of the local heat transfer coefficient. Using conservation of energy, the convective heat flux is equal to the conductive flux through the aluminium plate. From Fourier's law of heat conduction, the heat flux can be determined if the temperature gradient at the surface is known in the plate. The approach was to place a series of thermocouples along the impinging surface and use a thermal imaging camera to get the profile on the back surface. Using a finite difference scheme, the temperatures in the aluminium plate could be estimated and the temperature gradient at the surface found. From this, the heat transfer coefficient and Nusselt number is found. Figure 21 shows a diagram for the experiment and the location of each thermocouple. A long pipe was used such that the flow was fully developed. To avoid any error in heat loss from the plate to

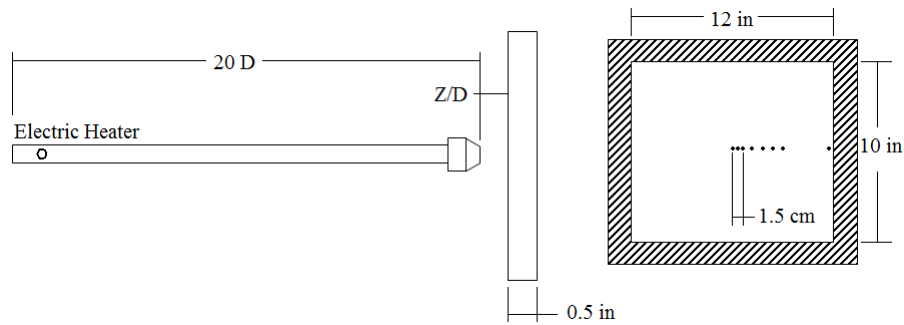


Fig. 21. Experimental setup for conjugate impinging jet.

the environment, the sides were insulated and only the front and back surfaces were exposed. Also the jet air was heated instead of the plate to avoid the need to quantify any loss to the environment as the plate cooled.

Several issues developed during the experimental study. First, it was too difficult to calibrate the thermal imaging camera to each thermocouple. The camera tended to recalibrate in between runs, and sometimes during the runs themselves. Attempts were made to quantify the emissivity of the aluminium surface, which was painted black and roughened, however the error between the thermal image and the thermocouples was still 10-15% and became worse with each run. This was likely due to insufficient time to allow the plate to cool to room temperature. It was decided that the images for the back surface could not be used. Also, the choice of material played a role in how quickly the temperature distribution developed. Aluminium is considered a good conductor and reached a uniform temperature rather quickly. This made it difficult to capture any distributions on the surface. To solve this, the jet flow rate, temperature, and spacing were decreased to reduce the heat transfer rate.

After further review a more effective parameter to compare is the jet effectiveness, which is a dimensionless temperature distribution on the surface. Although

the experiment results were ultimately not used, they did provide some insight into aspects relevant to the computational study. Namely a choice of material. The ratio between the solid and fluid thermal diffusivity needs to remain constant, but to speed up the time of the computation the individual properties of each can be altered.

Due to the errors in the experiment, a case that did not consider CHT was selected as a benchmark. This was the study done by Peet et al [19]. Although Peet did not consider CHT, it was a film cooling hole study that could be compared against a case that did consider CHT. Also Peet collaborated with the experimentalists to obtain the entire data distribution and provided the data density needed for comparison.

CHAPTER III

RESULTS

The following section gives details of the current study progress. An adiabatic and a conjugate case were run to compare to the experiments of Pietrzyk [14] and Sinha [18]. Currently, the conjugate case has not reached a steady thermal equilibrium that would yield any confident and consistence results. To accelerate the conjugate simulation to a statistically steady point, the simulation is run using a lower polynomial basis set. Although this is temporarily not a DNS, both the CFL criterion is relaxed (larger time steps) as well a reduction in total operation count per time step. Once the statistically steady state is approached, resolution is increased to appropriate values as tested by a convergence check. The coarser mesh may filter out smaller eddy structures, but should still give an idea of average values comparable to the experiments and adiabatic case. Any issues in resolution seen in the adiabatic convergence study will be used pro actively for the conjugate case. As the mesh is refined it may pick up flow structures that have been filtered by the coarser grid, resulting in the unusual shape in the convergence plot.

The total combined run time for both cases to this point is approximately 100,000 CPU hours. The adiabatic case was run with 504 processors on Kraken supercomputer at the University of Tennessee. The conjugate case is run on 128 processors using Texas A&M supercomputer Hydra.

A. Convergence Study

A convergence study was performed to check the consistency and stability of the adiabatic case. The results are shown in Figure 22. The plot exhibits exponential convergence until polynomial order 14 where there is a spike in error. There are

several possible reasons for this behaviour. The most likely cause is the flow field is under-resolved in some area near the film cooling jet and free stream boundary layer interaction.

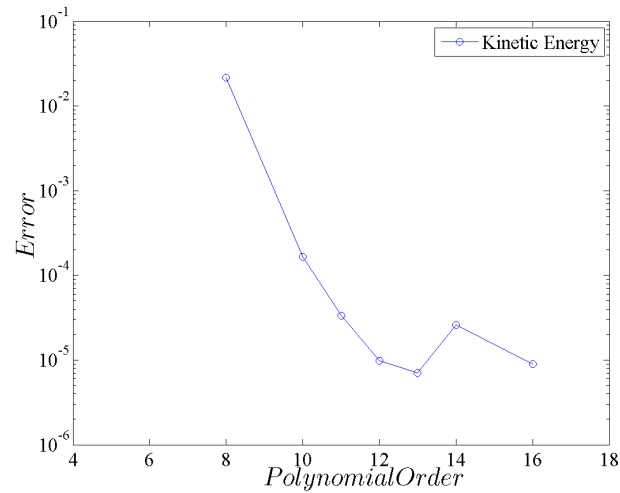


Fig. 22. Convergence plot for adiabatic case. Integral parameter chosen to be total energy within a volume containing film cooling hole exit. Reference state taken to be order 18.

The likely structure is the ‘downstream spiral separation node’ (DSSN) that occurs at the trailing edge of the film cooling hole exit. At the leading edge of the film cooling hole, the free stream boundary layer stagnates against the exiting film jet creating a horseshoe vortex that wraps around the hole in the stream wise direction. Some of this vorticity is entrained by cross flow that wraps around the back of the hole and settles under the jet exit. Peet et al [19] visualized this structure by plotting mean velocity stream lines, and appears in Figure 23. This structure reduces the local film cooling effectiveness by: aiding the jet film separation from the hole’s trailing edge, and trapping hotter free stream gas under the jet. This effect can be seen in Figure 24 by the local drop in film cooling effectiveness reported by Peet [19]. The adiabatic

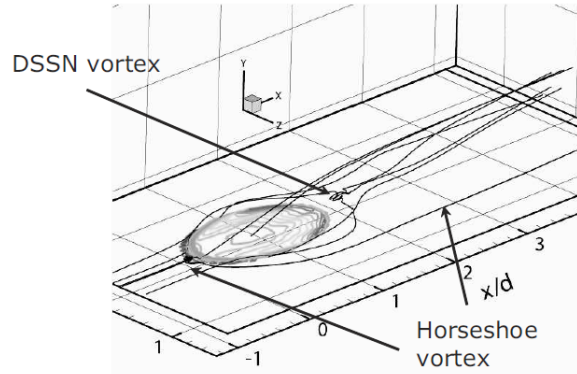


Fig. 23. Downstream spiral separation node vortex. Visualization around film cooling hole exit taken from Peet [19].

case does not appear to capture this structure by comparison.

Refining the mesh in the near hole region will resolve this structure. Another convergence check will be done to ensure consistency and stability of the new mesh.

B. Average Velocity Profiles

Average velocity profiles reported by Pietrzyk et al. [14] and summarized by Peet appear in this section. The velocity profiles at different locations can give details about the flow structure exiting the film cooling hole. Figure 24 shows velocity profiles at the film cooling exit (at the free stream - cooling hole interface). The two images give stream wise and span wise profiles in the hole exit. Comparison of the adiabatic DNS case shows fair agreement, however there are small fluctuations in the values presented which should improve with more averaged data.

In both instances, there is a velocity deficiency near the hole center represented by the “valley” in each profile. This is caused by flow separation that occurs in the film cooling hole. At the plenum exit, fluid near the trailing edge accelerates into the

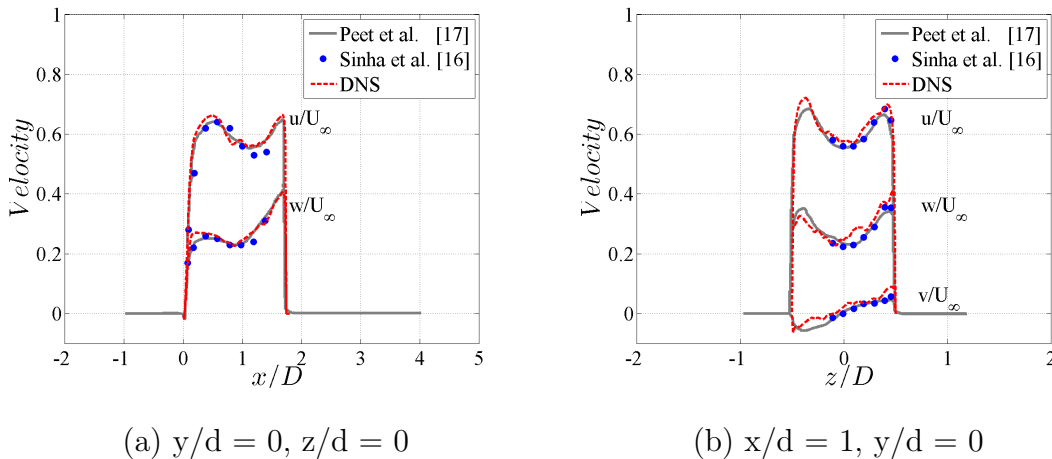


Fig. 24. Adiabatic film cooling hole exit velocity profiles. (left) shows stream wise profiles, and (right) shows span wise profiles.

film cooling hole and separates at the edge. This causes the flow velocity to increase near the leading edge, as shown in Figure 25.

This jetting effect causes the fluid at the film hole exit to be have a large velocity near the edges, with the smallest velocity coming at the trailing edge. This effect, combined with the sudden change in geometry, causes the film jet to separate at the trailing edge exit and reattach downstream of the DSSN vortex.

The DSSN vortex is more apparent in the conjugate case as shown in Figure 26, where mean velocity contours are shown to roll up under the jet detachment region. It is unclear why the DSSN vortex appears in the low order conjugate case, but may have to do with the blowing ratio and momentum flux ratio.

Figure 27 shows free stream velocity distributions for two locations just above the film cooling hole exit. The hole would be located from $x/d = 0$ to approximately $x/d = 1.8$. Two important features are visible that occur near the hole. Near the leading edge, the free stream component velocity drops suddenly due to the stagnating boundary layer with the jet exit and horseshoe vortex formation. The recovery in the

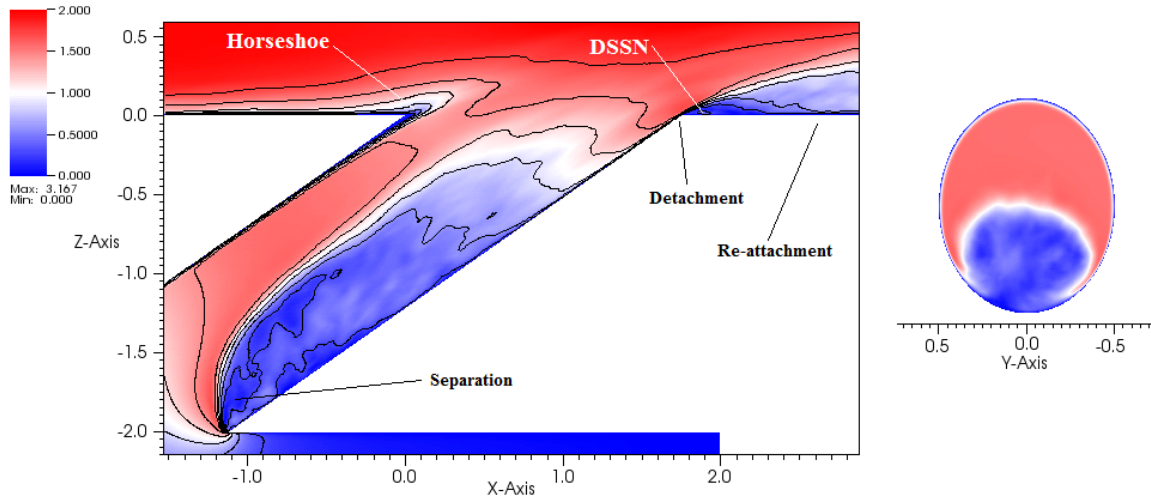


Fig. 25. Jetting phenomena in film cooling hole. This results from flow separation at the trailing edge of the plenum exit. Plot shows contours of velocity magnitude.

hole region is due to the addition of mass flow from the film jet. At the trailing edge of the hole there is a dramatic drop in velocity again due to the jet separating at the exit, from which it recovers downstream.

The adiabatic case again has fair agreement with the experiment, but appears to miss certain scales of motion by over or under predicting the velocity in certain areas. This is likely due to an unresolved region as suggested in the convergence study.

Span wise development of the velocity profiles appears in Figure 28. The two locations are at $x/d = 1$ (middle of film cooling hole) and $x/d = 5$. In each case the profiles are shown at a height above the endwall $z/d = 0.15$. Excellent agreement is seen for the span wise and normal velocity profiles, however the free stream velocity appears to over predict the experiments significantly in certain areas.

Looking at the left image, a distinct feature of film cooling holes can be seen by

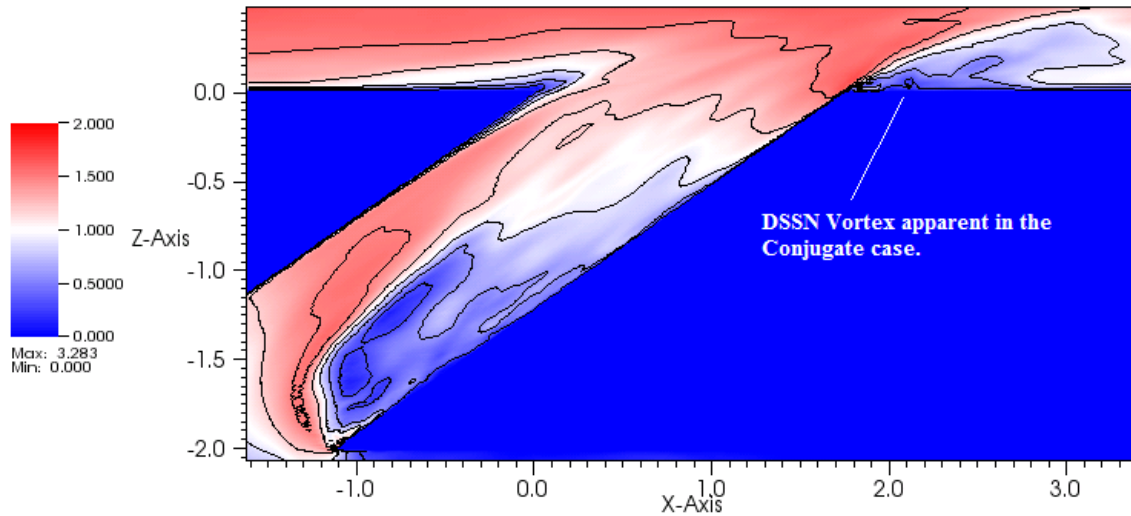


Fig. 26. DSSN vortex visible in conjugate case. Plot shows contours of velocity magnitude. The momentum flux ratio I determines the jet detachment behaviour, and may be different in the conjugate case due to the impinging jet.

the span wise velocity component ‘ v ’. Near the entrance to the film cooling hole in the plenum, fluid entering the hole “mushrooms” forming a pair of vortices called the Counter Rotating Vortex Pair (CRVP). This structure proceeds up the hole, and is carried down stream as it exits. The span wise velocity captures this by the equal and opposite direction shown in the profile. The cross flow at the hole exit points towards the centerline suggesting the presence of the CRVP. The CRVP reduces the film cooling effectiveness by pulling cool fluid into the freestream, and replacing it with hotter fluid.

C. Film Cooling Effectiveness

The following reports film cooling effectiveness values and temperature profiles for the adiabatic and conjugate cases. Figure 29 shows the average temperature distribution

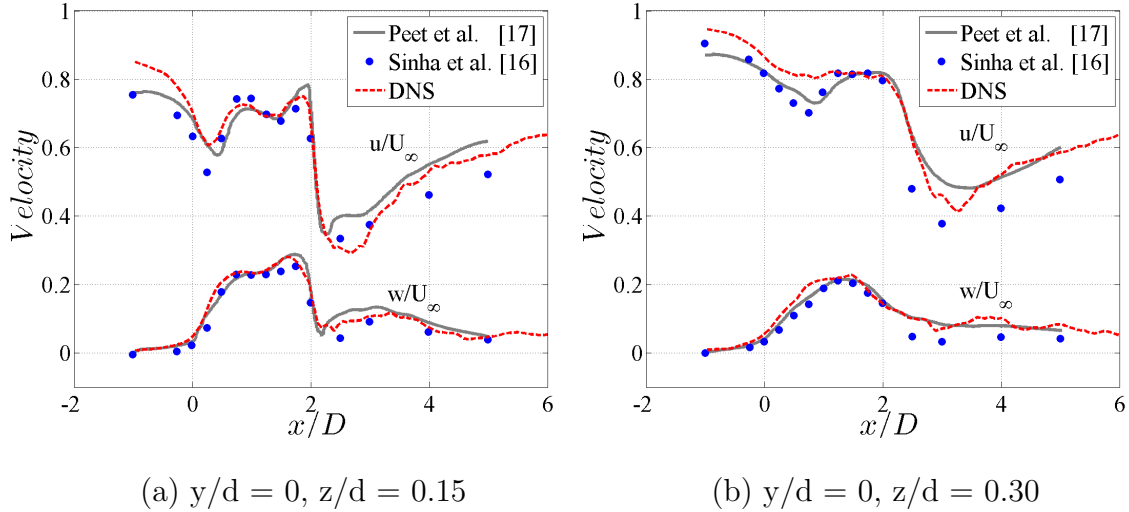


Fig. 27. Adiabatic film cooling hole free stream velocity profiles. (left) shows stream wise profiles at $z = 0.15$, and (right) shows stream wise profiles at $z = 0.30$.

at the wall. Examining the trailing edge region, there does not appear to be any local hot spots resulting from the DSSN vortex, or jet separation.

Figure 30 shows the centerline temperature distribution of the film jet for the adiabatic case. Again there does not appear to be any vortex structure apparent at the trailing edge. The result, or the ‘lack’ of the vortex may be the cause of the convergence study issues and the film cooling effectiveness values discussed below.

For the conjugate case, Figure 31 shows an averaged temperature distribution in the solid endwall. Localized cooling near the impinging jet can be seen. As the impinging jet removes heat from the underside, it moves through the plenum and continues to remove heat through entering the cooling hole. By this time the jet temperature has received some heat that reduces its effectiveness in film cooling. A balance must be made between the jet flow rate into the plenum such that it cools the underside while still providing desirable film cooling.

Peet et al. [19] organized data from Sinha [18] and reported film cooling effective-

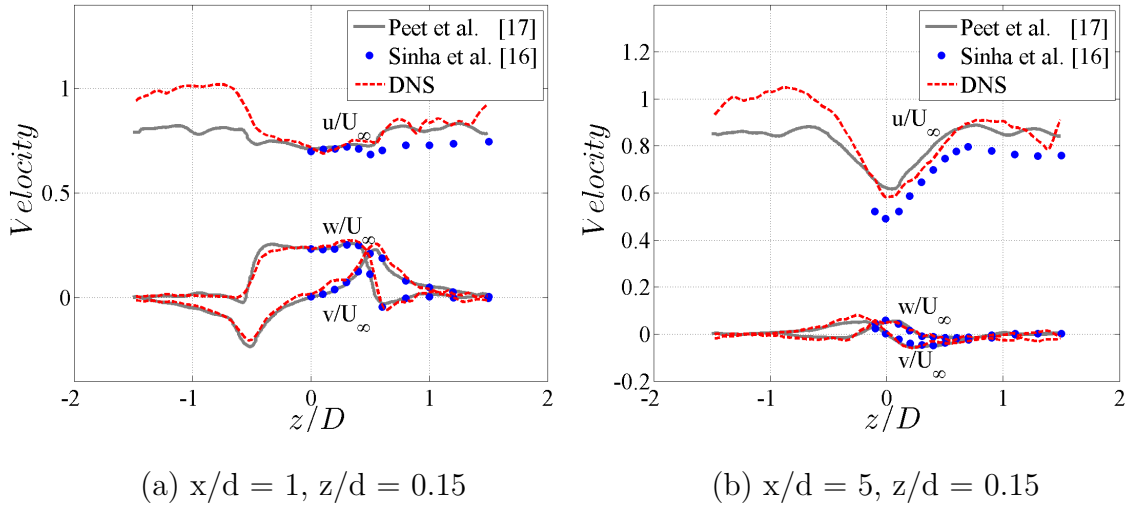


Fig. 28. Development of span wise velocity profiles. (left) shows span wise profiles at $x/d = 1$, and (right) shows span wise profiles downstream at $x/d = 5$.

ness at three areas: Centerline effectiveness in the stream wise direction, a laterally averaged stream wise effectiveness, and a span wise effectiveness downstream of the hole. Each location effectiveness appears in Figure 32.

In all cases, the preliminary conjugate results show large differences and appear constant. This confirms that the case has yet to reach a steady thermal point and needs to continue to run as a low order case. There is poor agreement for the adiabatic case centerline effectiveness. The experiment by Sinha et al. did not report any values less than $x/d = 2.74$, however the effectiveness is expected to drop near the leading edge due to jet detachment and the DSSN vortex structure as reported by Peet. The laterally averaged figure shows better agreement, but over predicts the experiments slightly and again does not show the diminished effectiveness near the exit. The over estimate can better be seen in the span wise effectiveness.

Some possible reasons for the differences could be the turbulence intensity levels, or the incoming flow field did not match the experiments. Also, it is important to

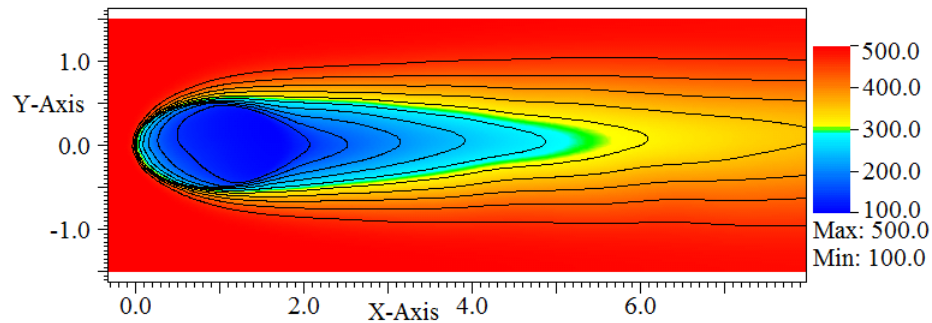


Fig. 29. Average adiabatic temperature distribution at the wall. Plot shows contours of Temperature. There does not appear to be any hot regions near the trailing edge resulting from the DSSN vortex.

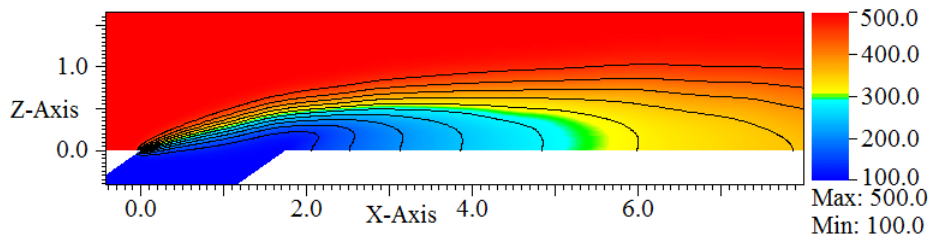


Fig. 30. Adiabatic temperature distribution at centerplane.

point out that the experiments by Sinha used a density ratio of 1.2, higher than the current study. Varying the density will be considered in the larger study.

Intensity levels recorded in the free stream for the adiabatic case were 2% whereas the experiments reported intensity levels less than 0.5%. The larger value in the simulation is a result of the intensity check routine, however viscosity does not appear to dampen out the level as the flow moves down stream compared to higher intensity levels. The intensity has been shown to effect cooling hole effectiveness, and a slight difference in intensity may skew the results. To solve this, the simulation's intensity check needs to be lowered such that the free stream intensity is matched.

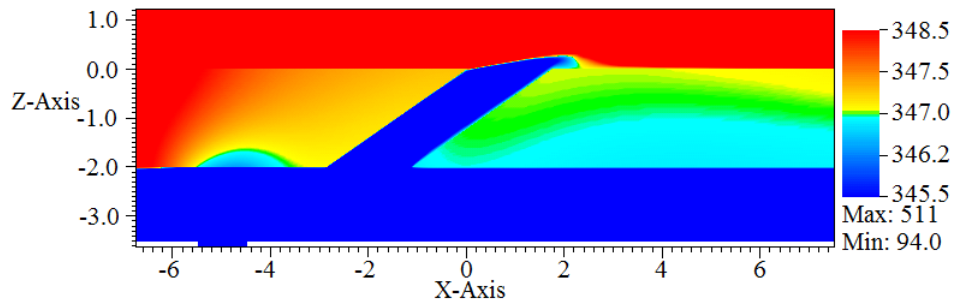


Fig. 31. Temperature distribution in the endwall conjugate case.

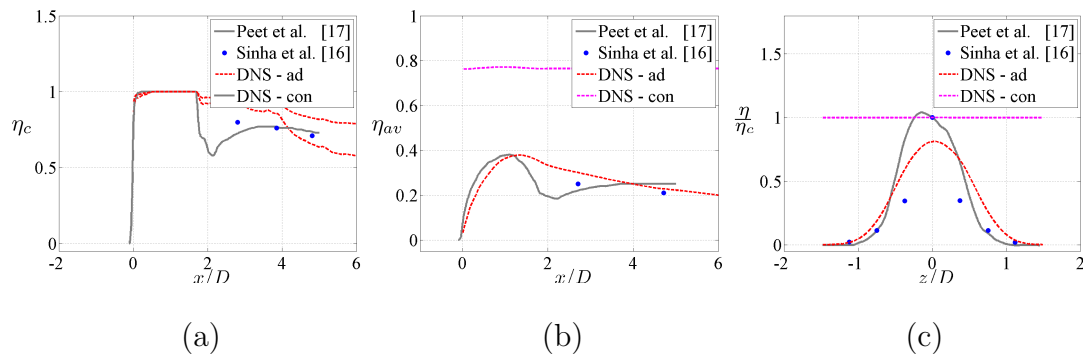


Fig. 32. Film cooling effectiveness comparisons. (left) Average center line Effectiveness, (middle) Laterally Averaged Effectiveness, and (right) Spanwise development at $X/D = 2.74$

The boundary layer parameters of the incoming flow field showed good agreement to the experiments, however the various flow ratios are larger than experiments. The VR, B, and I ratios were all too large and may effect the detachment region downstream of the hole. This could have an effect on the cooling effectiveness. To solve this, the inlet velocity to the plenum needs to be adjusted.

The most probable cause of error is under resolving the flow field in the near wall region of the film cooling hole exit. The effects of this were noticeable in the convergence study and need to be addressed by refining the trailing edge region to

capture the DSSN vortex and jet reattachment.

D. Future Considerations

Work that needs to be done can be described in terms of the current study, and the larger study. The larger study will add levels of complexity that builds off the current adiabatic and conjugate cases.

1. Current Study

The most pressing issue for the current study is further resolving the flow around the film cooling hole's leading and trailing edges. It is believed that the DSSN vortex that forms at the trailing edge degrades film cooling effectiveness and the convergence study suggests that this may be a flow structure that is under resolved. Further, the film cooling effectiveness does not show good agreement as a possible result.

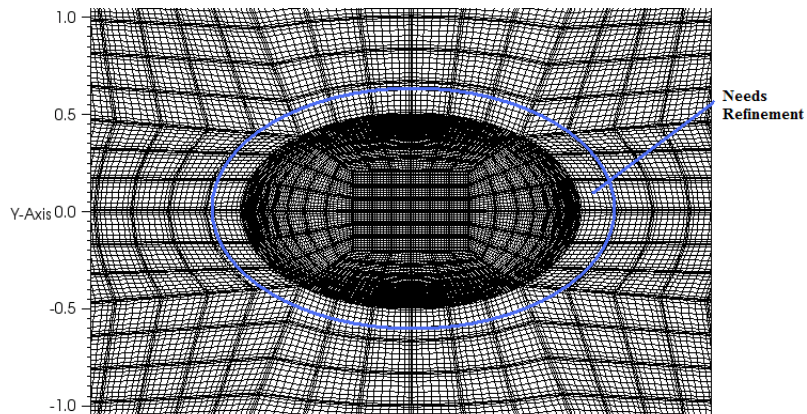


Fig. 33. Near wall mesh around film cooling hole. The mesh needs refinement in the area shown.

The inflow generation technique also needs to be addressed as there were issues with the boundary layer parameters reported in chapter 2. The momentum ratio may

effect jet detachment in the film cooling regime which would influence the formation of the DSSN vortex. It is possible that the vortex is simply not being formed. The density ratio will remain constant for this study, but will be varied in the larger study. The turbulence intensity in the free stream needs to be dampened to lower it to the experimental value. After this, another convergence study will be performed to ensure that the issues have been resolved.

For the conjugate case, the simulation will continue to be run until a statistically steady state has been reached. Currently the thermal equilibrium in the solid region has not occurred, and the case is running as a low polynomial order basis. When the case has reached a steady thermal state, a scaling and convergence study will be done to determine the processors and grid resolution for production runs.

2. Larger Study

The future study will simulate a full turbine vane and film cooling hole arrangement that characterizes and reduces flow losses. It will consider a contoured endwall, conjugate heat transfer, variable density ratios, and high free stream turbulence and large length scales typical of combustor exit profiles. The objective is to reduce the secondary flows that occur along the endwall that compete against film cooling by simulating a realistic environment. The simulation will be done as a LES with engine conditions. An example of the configuration for the future study appears in Figure 34.

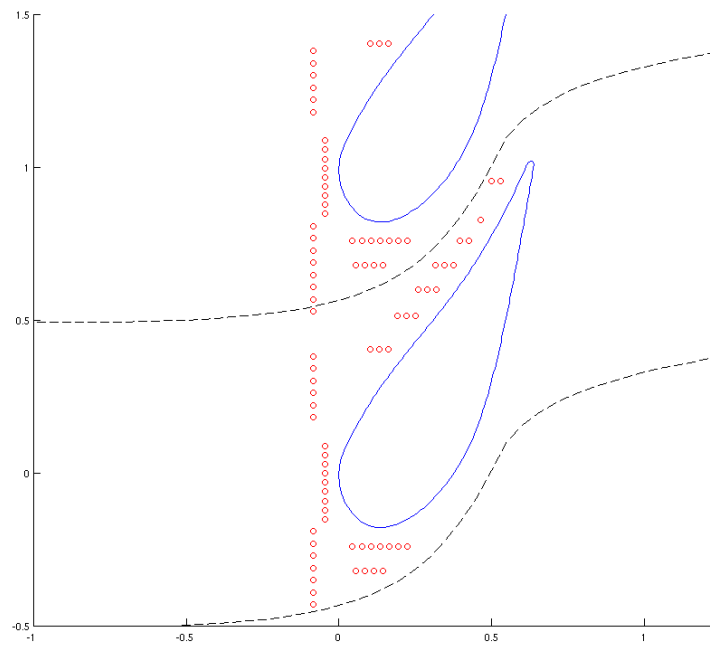


Fig. 34. Future simulation domain. Cooling holes are represented as red, the turbine vane as blue. The black dashed lines represent the periodic domain for the simulation.

CHAPTER IV

CONCLUDING REMARKS

The improved performance of Gas turbines is closely tied to improvement in cooling technologies. Modern gas turbine engines have made vast improvements in efficiency by raising the exhaust gas temperature of the combustor. To do this, cooling technologies needed to be developed to protect the materials from thermal stresses during prolonged operations.

Any continued advancement in gas turbines demands further improvement in cooling techniques. To do this, a complete picture of the flow field and secondary flows with realistic engine conditions is needed. Many techniques used to cool the turbine endwall depend on the structure of the secondary flows. To characterize them, a complete vane simulation will be done that considers conjugate heat transfer, variable density ratios, large turbulence intensity and length scales representative of combustor exit profiles, and Reynolds numbers based on engine conditions. Also, a contoured end wall will be done to examine the effect on reducing the secondary flows.

Before this can be done, the present study was conducted to answer issues that may develop. This study reported good agreement with average velocity profiles presented by experiments, however the adiabatic film effectiveness did not match up well. Two reasons are thought to cause this. The first is the momentum flux ratio which influences the jet film detachment, and may interfere with the formation of the DSSN vortex at the cooling hole's trailing edge. Second, a convergence study was done that showed good convergence up to polynomial basis order 14 from which the error jumps back up. It was thought that this implies the flow may be under resolved in some area.

However, the conjugate case did show a presence of the DSSN vortex suggest-

ing that the resolution may not be an issue as previously thought since this case is currently running as a low polynomial order basis. The momentum flux ratio in the conjugate case is less than the adiabatic case, and may play a role to the formation of this vortex. The adiabatic case will need to be adjusted to improve the boundary condition ratios and boundary layer parameters. The area around the film cooling hole exit will also be refined and a second convergence study done.

When the conjugate case has reached a statistically steady point, a grid refinement study will be done to determine a suitable grid resolution for production runs. The effectiveness values for the current state confirmed that the case has not reached a thermal equilibrium as the average effectiveness values appear constant. Once steady, velocity profiles, turbulent statistics, and average film cooling effectiveness values will be reported to compare to the adiabatic case. The results will be used as a benchmark for the larger study.

REFERENCES

- [1] Rolls-Royce, *The Jet Engine*. London, England: Rolls-Royce, 2005.
- [2] F. Ames, “The influence of large-scale high-intensity turbulence on vane heat transfer,” *Journal of Turbomachinery*, vol. 119, no. 2, pp. 23–30, Jan. 1997.
- [3] M. Schobeiri, *Turbomachinery Flow Physics and Dynamic Performance*. Berlin: Springer-Verlag, 2005.
- [4] L. Langston, “Crossflows in a turbine cascade passage,” *Journal of Engineering for Power*, vol. 102, no. 4, pp. 866–874, Mar. 1980.
- [5] C. Smith and D. Sabatino, “Boundary layer influence on the unsteady horseshoe vortex flow and surface heat transfer,” *Journal of Turbomachinery*, vol. 132, no. 1, p. 011015, Jan. 2009.
- [6] A. Lethander, K. Thole, G. Zess, and J. Wagner, “Vane-endwall junction optimization to reduce turbine vane passage adiabatic wall temperatures,” *Journal of Propulsion and Power*, vol. 20, no. 6, pp. 1105–1116, Dec. 2004.
- [7] J. Han, J. Park, and C. Lie, “Heat transfer and pressure drop in blade cooling channels with turbulence promoters.” Final Report Texas A&M Univ., College Station. Dept. of Mechanical Engineering. (prepared for NASA CR-3837), 1984.
- [8] J. Han, S. Dutta, and S. Ekkad, *Gas Turbine Heat Transfer and Cooling Technology*. New York, NY: Taylor & Francis, 2000.
- [9] B. Hollworth and L. Dagan, “Arrays of impingement jets with spent fluid removal through vent holes on the target surface. Part I: Average heat transfer,” *Journal of Engineering for Power*, vol. 102, pp. 994–999, Mar. 1980.

- [10] J. Han and S. Dutta, “Internal convection heat transfer and cooling: an experimental approach..” von Karman Institute for Fluid Dynamics, Lecture Series 1995-05 on Heat Transfer and Cooling in Gas Turbines, Belgium, May 8-12, 1995.
- [11] G. Kool, “Current and future materials in advanced gas turbine engines,” *Journal of Thermal Spray Technology*, vol. 5, pp. 31–34, Mar. 1996.
- [12] T. Khan and P. Caron, “Advanced superalloys for turbine blade and vane applications.” CIM Symposium on ‘Advances in Gas Turbine Engine Materials’, Ottawa, Ontario, August 19-20, 1991.
- [13] D. Bogard and K. Thole, “Gas turbine film cooling,” *Journal of Propulsion and Power*, vol. 22, no. 2, pp. 249–270, Apr. 2006.
- [14] J. Pietrzyk, D. Bogard, and M. Crawford, “Hydrodynamic measurements of jets in crossflow for gas turbine film cooling applications,” *Journal of Turbomachinery*, vol. 111, no. 2, pp. 139–145, Apr. 1989.
- [15] L. Wright, S. McClain, and M. Clemenson, “Effect of freestream turbulence intensity on film cooling jet structure and surface effectiveness using PIV and PSP,” *ASME paper GT2010-23054*, 2010.
- [16] K. Kadotani and R. Goldstein, “Effect of mainstream variables on jets issuing from a row of inclined round holes,” *Transactions of the American Society of Mechanical Engineers*, vol. 101, pp. 298–304, Apr. 1979.
- [17] G. Jumper, W. Elrod, and R. Rivir, “Film cooling effectiveness in high turbulence flow,” *Journal of Turbomachinery*, vol. 113, no. 3, pp. 479–483, Dec. 1991.

- [18] A. Sinha, D. Bogard, and M. Crawford, “Film-cooling effectiveness downstream of a single row of holes with variable density ratio,” *Journal of Turbomachinery*, vol. 113, no. 3, pp. 442–449, 1991.
- [19] Y. Peet and S. Lele, “Near field of film cooling jet issued into a flat plate boundary layer: Les study,” *ASME paper GT2008-50420*, 2008.
- [20] A. Dorfman, *Conjugate Problems in Convective Heat Transfer*. Boca Raton, FL: CRC, 2010.
- [21] K. Harrison and D. Bogard, “Use of the adiabatic wall temperature in film cooling to predict wall heat flux and temperature,” *ASME Turbo Expo*, vol. 4, pp. 1197–1207, 2008.
- [22] R. Fox, A. McDonald, and P. Pritchard, *Introduction to Fluid Mechanics*, pp. 412–413. Danvers, MA: John Wiley and Sons, Inc., 2004.
- [23] O. Walsh, “Eddy solutions of the Navier-Stokes equations,” *Lecture Notes in Mathematics*, vol. 1530, pp. 306–309, 1992.

VITA

Charles Michael Meador was born August 17, 1986 to Bonnie and Chuck Meador in Houston, Texas. He grew up living outside of Houston attending school in Cypress Fairbanks where he graduated in 2004. From there he moved to College Station, Texas to study mechanical engineering at Texas A&M University. During his time at the university he completed four internships with Schlumberger. During one of these internships he met his wife, Angelica Meador, who was studying industrial engineering at the University of Florida and interning at the same company. After graduating with a B.S. in mechanical engineering in the spring of 2009 he joined the graduate program at Texas A&M to pursue a M.S. in the Fluids, Turbulence, and Fundamental Transport Lab headed by Professor Dr. Andrew Duggleby. He received his M.S. in December of 2010 and plans to stay in the same group to pursue a Ph.D in mechanical engineering. His permanent address is:

Texas A&M University
Department of Mechanical Engineering
3123 TAMU
College Station TX 77843-3123

The typist for this thesis was the author.